Universiteit Leiden
The Netherlands

From star-formation to recombination: expanding our view of the radio recombination line universe

Emig, K.L.

Citation
Emig, K. L. (2021, April 29). *From star-formation to recombination: expanding our view of the radio recombination line universe*. Retrieved from https://hdl.handle.net/1887/3160759

Version:	Publisher's Version
License:	Licence agreement concerning inclusion of doctoral thesis in the Institutional Repository of the University of Leiden
Downloaded from:	https://hdl.handle.net/1887/3160759

Note: To cite this publication please use the final published version (if applicable).

Cover Page

Universiteit Leiden

Leiden University Repository

The handle https://hdl.handle.net/1887/3160759 holds various files of this Leiden University dissertation.

Author: Emig, K.L.
Title: From star-formation to recombination: expanding our view of the radio recombination line universe
Issue Date: 2021-04-29

2 | Low-Frequency Observations of Diffuse Ionized Gas in Cygnus X

Abstract

Photoionized gas probes the influence of massive stars on their environment. The Cygnus X region ($d \sim 1.5$ kpc) is one of the most massive star forming complexes in our Galaxy, in which the Cyg OB2 association (age of 3-5 Myr and stellar mass 2×10^4 $M_\odot$) has a dominant influence. We observe the Cygnus X region at 142 MHz using the Low Frequency Array (LOFAR) and take into account short-spacing information during image deconvolution. Together with data from the Canadian Galactic Plane Survey, we investigate the morphology, distribution, and physical conditions of low-density ionized gas in a $4^\circ \times 4^\circ$ ($\sim$100 pc $\times$ 100 pc) region at a resolution of $2'$ (0.9 pc). The radio emission in the region analyzed is almost entirely thermal (free-free) at 142 MHz, with emission measures (EM) of $10^3 < EM$ [pc cm^{-6}] $< 10^6$. As filamentary structure is a prominent feature of the emission, we use `DisPerSE` and `FilChaP` to identify filaments and characterize their radial (EM) profiles. The distribution of profiles has a characteristic filament width of 3.6 pc and a power-law distribution ($\beta = -1.8 \pm 0.1$) in peak EM down to our completeness limit of 4200 pc cm^{-6}. The electron densities in the filaments range between $10 \lesssim n_e$ [cm^{-3}] $\lesssim 400$ with a median value of 38 cm^{-3}, remarkably similar to [N II] surveys of ionized gas. Cyg OB2 may ionize up to two-thirds of the total ionized gas and the ionized gas in filaments. Indeed we find the majority of filaments are likely photoevaporating surfaces flowing into a surrounding diffuse ($\sim$5 cm^{-3}) medium. However, stellar winds of Cyg OB2 may create a minority of the ionized filaments through dissipated turbulence or shock heated ionized gas. We discuss Cygnus X as a source of "extended low-density" (ELD) ionized gas; this gas is not well confined to the region, but can be replenished over the lifetime of Cyg OB2 by ten of the typical photoevaporating filaments we characterize.

K. L. Emig, G. J. White, P. Salas, R. L. Karim, R. van Weeren, P. Teuben,
H. J. A. Röttgering, A. G. G. M. Tielens, *et. al*

to be submitted to Astronomy & Astrophysics

2.1 Introduction

The interaction of massive stars with their environment has a profound impact on the evolution of galaxies (Hopkins et al. 2014, 2018) through the collective effects of protostellar outflows (Bally 2016), ionizing radiation (Matzner 2002), stellar winds and supernovae (SN; Yorke et al. 1989). One way to investigate their impact is through photoionized gas, in which stars of mass $M_\star \gtrsim 7$ M$_\odot$, all O types and earlier than B3, produce extreme ultraviolet (EUV) radiation of $E \geq 13.6$ eV capable of photoionizing hydrogen in the surrounding medium.

Early in their lifetimes, massive stars dissociate and ionize their immediate environment. Dense H II regions form as pockets of ionized gas, increasing the thermal gas pressure within the molecular cloud by three orders of magnitude. The subsequent expansion of an H II region can mechanically unbind the parent cloud and induce turbulent motions (e.g., Walch et al. 2012) in the interstellar medium (ISM). As an H II region grows, its volume density diminishes. Stellar winds and radiation pressure are also important contributors to the expansion of the ionized gas volume (e.g., Pabst et al. 2019, 2020; Olivier et al. 2020). As a result of peculiar motion and/or inhomogeneities in the medium, within a few Myr (e.g., Mezger 1978), the star, its photons and the gas it ionizes enter a surrounding low-density ($n_e \sim 0.1 - 100$ cm^{-3}) medium.

Within the plane of the Galaxy, photoionized gas is found in a variety of environments (and referred to with a variety of different names). Dense ($n_e > 10^3$ cm^{-3}) ionized gas pervades compact, ionization-bounded H II regions. From leaky H II regions, ionizing photons escaping through porous material create (partially) ionized gas ($1 - 10$ cm^{-3}) in the envelopes of H II regions; alternatively these envelopes may be ionized from the outside. Transitioning to density-bounded H II regions, ionized gas ($1 - 100$ cm^{-3}) permeates to larger volumes in blister H II regions aided by champagne flows (Tenorio-Tagle 1979) of ionized gas into lower-density regions. When stellar winds are influential in an H II region, the medium stratifies with ionized gas at larger radii and hot gas filling the inner regions (Weaver et al. 1977; Churchwell et al. 2006). Assisted by supernova explosions, massive stars create large excavated regions or plasma tunnels containing fully ionized gas ($1 - 10$ cm^{-3}). Over-pressured — thus denser, brighter, and more readily detected — photoevaporating ionized gas (of smaller path length) is frequently observed in a number of these scenarios as ionization fronts propagate into local neutral material. Ionizing photons which escape in these scenarios provide a surplus of the ionizing photon budget required to maintain (e.g., Reynolds 1984) the pervasive (volume filling factor $\phi \sim 0.25$, Kulkarni & Heiles 1988) warm ionized component of the ISM (WIM), that resides both in the Galactic plane ($n_e \sim 0.1$ cm^{-3}) and which is characterized by large ($z \sim 1$ kpc) scale heights (for a review see Haffner et al. 2009).

Blind surveys and large targeted samples with thermal radio continua (Mezger 1978; Murray & Rahman 2010), radio recombination line emission (Shaver 1976; Lockman 1976; Anantharamaiah 1985b, 1986; Roshi & Anantharamaiah 2000; Heiles et al. 1996b; Alves et al. 2015), FIR fine structure line emission from [N II] (Bennett et al. 1994; Goldsmith et al. 2015) and pulsar dispersion measures (Berkhuijsen et al. 2006, and references therein) have brought to light properties of low-density ionized gas

within the Galactic plane. Mezger (1978) estimated that 84% of ionizing photons are emitted by O stars outside of compact H II regions, in gas characterized by densities of $n_e \approx 5-10$ cm^{-3} dubbed extended low-density (ELD) H II gas. However, a number of different conclusions have been reached regarding the dominant origin of this gas: (i) envelopes of H II regions (Shaver 1976; Anantharamaiah 1986; McKee & Williams 1997), (ii) a pervasive component (Heiles et al. 1996b) which may be a continuation of the WIM (Bennett et al. 1994; Berkhuijsen et al. 2006), and (iii) from just a handful of the most luminous sources (Murray & Rahman 2010). High-resolution pinhole surveys of FIR fine structure lines (Goldsmith et al. 2015; Pineda et al. 2019) trace somewhat denser gas (with mean values of $n_e \approx 30 - 40$ cm^{-3}) and could plausibly be tied with these three possibilities.

The detailed nature of low-density gas has been revealed in individual nebulae, some of which show ridge-like and filament morphologies. For example, IC 434, the ionized gas associated with the Horsehead area in Orion, is a low-density (~ 100 cm^{-3}) ionization front created by an O star (σ Ori) drifting away (Ochsendorf et al. 2014). The California Nebula (NGC 1499) is low-density ionized gas created as a chance encounter with a run away star (Bohnenstengel & Wendker 1976). Barnard's Loop is low-density ($\sim$3 cm^{-3}) ionized gas swept up and transported away by a SN explosion within the Orion-Eridanus bubble and ionized by the Orion Belt stars whose ionizing photons can travel some 10's of pc inside the Orion-Eridanus bubble (Ochsendorf et al. 2015; Abdullah & Tielens 2020). The massive Arches star cluster, in a region dominated by stellar winds, maintains the prominent photoionized Arched Filaments (Lang et al. 2001).

The Cygnus X region is a massive complex which also displays filamentary-like structure in low-density ionized gas (Wendker et al. 1991). "Cygnus X" refers to a $\sim$10° wide region in the galactic plane with enhanced radio emission (Piddington & Minnett 1952) – for an overview of the region see Reipurth & Schneider (2008). This coherent region of massive star formation appears to lie at $\sim$1.5 kpc (Schneider et al. 2006; Rygl et al. 2012) and dominates the observed emission, despite the view looking down a spiral arm in this direction. Open and massive OB associations are seen in this direction at a similar distance – Cyg OB1, OB2, OB6, OB9 (Uyaniker et al. 2001). Yet (a subset of) the region still retains a large reservoir ($M > 10^6$ M$_\odot$) of molecular gas (Schneider et al. 2006, 2011). Massive post main-sequence stars indicate that star formation began in the region $\sim$15 Myr ago (Comerón & Pasquali 2012; Comerón et al. 2016, 2020). Though the nature of the rarefied region is debated, it is consistent with the superbubble formalism (Mckee & Ostriker 1977) indicating that stellar winds and/or supernovae have contributed to excavating the parent cloud(s) (Bochkarev & Sitnik 1985; Ackermann et al. 2011).

Part of the region that is referred to as Cygnus X North (Schneider et al. 2006) harbors Cyg OB2 and other smaller clusters and associations, some of which are actively forming stars (Cong 1977; Odenwald et al. 1990; Comeron & Torra 1999; Comerón & Torra 2001; Le Duigou & Knodlseder 2002; Marston et al. 2004; Motte et al. 2007; Beerer et al. 2010; Panwar et al. 2020). The Cyg OB2 association strongly influences the medium, largely characterized through pillars and globules (Wright et al. 2012; Schneider et al. 2016; Deb et al. 2018). Cyg OB2 has a total stellar mass of $M_\star = 1.7^{+0.4}_{-0.3} \times 10^4$ M$_\odot$ (Wright et al. 2015). It is not bound gravitationally and

likely formed that way, in a relatively low density environment given its mass (Wright et al. 2014), during bursts of star formation 3 and 5 Myr ago (Wright et al. 2010; Berlanas et al. 2020).

In this article, we investigate low-density ionized gas in Cygnus X (North) with 142 MHz continuum observations using the Low Frequency Array (LOFAR; van Haarlem et al. 2013). We observe this region, encompassing 16 square degrees ($\sim$10 kpc^2) within a single pointing, around the Cyg OB2 association as it contains a wide variety of evolutionary stages of star-formation with low-density ionized gas. We aim to characterize the influence of massive stars on their environment and explore the connection between low-density ionized gas and ELD H II gas. This is the first analysis with LOFAR which focuses on (extended) thermal emission in the Galactic plane.

We adopt a distance of $d = 1.5 \pm 0.1$ kpc to the Cygnus X region and Cyg OB2 following (Comerón et al. 2020, see their Sec. 2.2 for a detailed discussion). After an analysis of molecular line emission linked the region as a coherent structure influenced by Cyg OB2 (Schneider et al. 2006, 2016), the distance to the Cygnus X complex was determined as 1.40 ± 0.08 kpc through maser observations of massive stars (Rygl et al. 2012). A recent *Gaia* analysis (Berlanas et al. 2019) places a main subgroup (80% of the OB population) of Cyg OB2 at $1.76^{+0.37}_{-0.26}$ kpc with a smaller subgroup at 1.35 ± 0.2 kpc. While a clear separation in distance distinguishes these two subgroups, Comerón et al. (2020) points out that a systematic offset in parallax may affect (both of) the distance determinations. At $d = 1.5$ kpc, the physical scale is $1' \approx 0.44$ pc.

2.2 Data

2.2.1 LOFAR observations & data processing

In this section we describe the data processing of LOFAR interferometric observations of one pointing centered approximately on the massive star forming region DR 21 at $(\alpha_{\rm RA}, \delta_{\rm dec}) = (309.5500°, +42.0708°)$ in J2000 coordinates. These data were obtained with the high band antennas (HBA) covering 110–190 MHz on July 19, 2013 under project LC0_032 (PI: G. White). Continuous frequency coverage was obtained between 126 – 165 MHz. 23 stations of the full Dutch array recorded data during these observations, which have a maximum baseline of 120 km (4″) and minimum baseline lengths of 70 m corresponding to largest angular scales of 96′ (1.6°). The on-source integration time is 6 hours and 50 minutes.[1] In this analysis, we make use of 2 MHz bandwidth that is split across 10 sub-bands and centered on 142 MHz. We use a small fraction (5%) of the available bandwidth and with our results, inform on the prospects that deeper LOFAR observations hold.

We recorded data throughout the observation also in the direction of Cygnus A (299.8682°, 40.7339°), a bright ($\sim 10^4$ Jy), well-modeled source 7.4° away from the target center. The flexibility of digitally pointing the LOFAR beam allows HBA data to be recorded towards multiple phase centers within the station beam of $\sim$20°. Because of the close proximity and simultaneous observation, we use Cygnus A as the

[1] A plot of the *uv* coverage of a typical LOFAR observation can be found in e.g., Figure 17 of van Haarlem et al. (2013).

primary calibrator source to derive flux, bandpass and phase calibrations to transfer to the target pointing.

Calibrating the visibilities

We describe the calibration of the visibility data in this section. We derive flux, bandpass and phase calibrations of the primary calibrator pointing. We then apply these to the target pointing. Lastly, we mitigate side lobe contribution from Cygnus A to the target pointing by subtracting Cygnus A visibilities from the target visibilities; the trade-off to LOFAR's large field of view is its susceptibility to strong side lobe contamination.

To begin processing of both the primary calibrator and target Measurement Sets (MS), we flag the correlations between the two "ears" of each HBA core station (van Haarlem et al. 2013) and flag for radio frequency interference (RFI) with `AOFlagger` (Offringa et al. 2012) at full time and frequency resolution (0.763 kHz channel) using the default HBA strategy (Offringa et al. 2012). We also flag station CS013 as its antennas were not properly phased up at the time of the observations. Then we average (by a factor of 64) the data to a channel resolution of 48.8 kHz. We run these steps using version 2.20_2 of the Default Pipeline Processing Platform (`DPPP`; van Diepen & Dijkema 2018). This version of `DPPP` outputs the data with minor updates to the metadata of the Measurement Set – as these data were recorded in Cycle 0 of LOFAR's operation – that are necessary in order to use later versions of `DPPP`. In subsequent processing, we make use of the most recent `DPPP` versions.

For the primary calibrator, we solve for the diagonal (XX and YY) gain, phase and amplitude, at full frequency resolution with `DPPP`. We use a LOFAR model of Cygnus A at 150 MHz consisting of 33 000 components (courtesy J. McKean; McKean et al. 2016). The solutions have cleanly converged, and they also indicate the ionosphere was relatively mild. We apply only the phase solutions. Then, we solve again for the diagonal gain, phase and amplitude. Using the LOFAR Solutions Tool (LoSoTo; de Gasperin et al. 2019), we flag spurious jumps in the amplitude solutions of each channel – likely due to instrumental instabilities – as well as any residual RFI, which are identified as 7σ outliers averaged over a sliding window of 40 solution intervals in time.

For the target pointing, we use `DPPP` to apply the phase solutions of the first iteration of gain calibration of the primary calibrator and both the amplitude and phase solutions of the second iteration. The time steps of the visibility data which have flagged amplitude solutions will be flagged as the solutions are applied. Phase offsets due to asynchronized — on the order of $\mathcal{O}$(10 nanoseconds) — station clocks of the remote stations (van Weeren et al. 2016) have been absorbed into the primary calibrator solutions. Furthermore, a calm ionosphere may be characterized by large patches of coherence in the total electron content (Intema et al. 2009), thus inducing similar phase errors (and Faraday rotation) towards the target and nearby primary calibrator. Phase (and amplitude) errors due to the ionosphere are absorbed into these solutions as well.

In the next step, we use `DPPP` to subtract Cygnus A from the target visibilities because of the close proximity of Cygnus A to our pointing center. We phase shift

the target visibilities to the location of Cygnus A and then predict the 33 000 source model of Cygnus A into the MODEL column. Next we smooth our visibilities with a baseline dependent averager (de Gasperin et al. 2019) and solve for the diagonal (XX and YY) gain at a 195.3 kHz frequency resolution and 1 minute time resolution, attempting to smear the visibility structure of the target. We corrupt the MODEL column with the solutions. Then we subtract the corrupted MODEL from the DATA. We phase-shift these visibilities back to the target phase center of the observation. In this manner, we have subtracted the off-axis signal of Cygnus A from the data. We find this approach produces more coherent solutions with a larger number of stations converging than with the standard "demixing" (van der Tol et al. 2007) capabilities of `DPPP`.

At this point, the target data are well calibrated against a source which has a peak flux 1000 brighter than the apparent flux of any source in the target field. We tested self-calibrating the data, in which we image (with the parameters specified in Section 2.2.1), create a sky model, and solve for an amplitude and phase calibration against the model. We see minor improvements for long baselines. However, our science aim is to investigate extended diffuse emission that is well characterized with low-resolution ($2'$) imaging. Self-calibration does not significantly improve our short baseline calibration. We thus opted not to perform the computationally intensive self-calibration.

Constructing a short-spacing map

The LOFAR data have excellent *uv* coverage to large scale emission with baselines as short as 70 m providing sensitivity to a largest angular size of $96'$. However, for observations near the Galactic plane, where large scale emission surpasses tens of degrees, information on the smallest *uv* scales is necessary to properly deconvolve and obtain the flux density of the extended $\mathcal{O}(1^\circ)$ structures in the Cygnus X region.

We construct a short-spacing map at 142 MHz and with $72'$ resolution that is interpolated from multi-frequency fits across 52 MHz, 408 MHz, 820 MHz, and 1420 MHz. To ensure that *uv* coverage of the short-spacing map overlaps with the *uv* coverage of the LOFAR observations, we targeted survey data with resolutions of approximately $\sim 1^\circ$ or less and which covered galactic latitudes of $|b| \lesssim 7^\circ$.

We compiled the following data. We make use of 52.224 MHz survey data obtained with the Owens Valley Radio Observatory Long Wavelength Array (OVRA-LWA; Eastwood et al. 2018). It has a native resolution of $16.2' \times 15.0'$ and an rms noise of 418 K. Inspection of the data in this region shows that it is calibrated to within $\sim$20% as compared to lower resolution surveys. We use the 408 MHz survey of Haslam et al. (1982) that has been de-stripped (to <1 K) of large-scale striations (Remazeilles et al. 2015). At 408 MHz, the data have a native resolution of $51'$, rms noise of 3.2 K, and zero level calibration of 3 K (Haslam et al. 1974). The 820 MHz survey with the Dwingeloo Telescope (Berkhuijsen 1972) has a native resolution of $72'$, rms noise of 0.2 K and zero level calibration of 0.6 K. The 820 MHz data limits the resolution of our frequency-interpolated map as it has the coarsest resolution of the data used. Lastly, the data used from the Stockert 25 m survey at 1420 MHz (Reich 1982) has a native resolution of $35'$, rms noise of 0.01 K and zero level calibration of 0.05 K.

The procedure we employ first involves creating an image cutout of $12^\circ \times 12^\circ$ centered on DR 21 from each survey. Then we smooth the cutouts to the common resolution of $72'$ and re-grid the images using CASA (McMullin et al. 2007; Emonts et al. 2019) to a common pixel grid and pixel size of $4.7'$. Next we convert the intensity scales from temperature brightness units to Jy beam^{-1}, as the imager we use, `wsclean` (Offringa et al. 2014; Offringa & Smirnov 2017), currently only accepts Jy units. Pixel by pixel, we fit a power-law[2] to the "high-frequency" data points at 408, 820 and 1420 MHz, as previous studies have found this region largely consists of thermal, free-free emission down to 408 MHz (Landecker 1984; Xu et al. 2013). Then, to the 52 MHz data point, we fit for either a free-free turnover or a synchrotron component. We do this by extrapolating the high-frequency fit to 52 MHz. If the flux density at 52 MHz is *less* than the extrapolated value of the fit at that frequency, we fit for a free-free turnover,

$$S(\nu) = \frac{S_{0,\mathrm{ff}}}{\tau_0}\left(\frac{\nu}{\nu_0}\right)^2\left(1 - \exp\left[-\tau_0\left(\frac{\nu}{\nu_0}\right)^{\alpha-2}\right]\right) \tag{2.1}$$

where α is the spectral index fit to high-frequency data, and $\nu_0 = 142$ MHz such that $S_{0,\mathrm{ff}}$ is the free-free component of the flux density at ν_0 in the optically thin (unabsorbed) regime and τ_0, the only free parameter in this fit, is the optical depth at ν_0. Otherwise, if the flux density at 52 MHz is *greater* than the extrapolated value of the power-law fit, we add-in a synchrotron component with spectral index -0.7 and fit,

$$S(\nu) = S_{0,\mathrm{ff}}\left(\frac{\nu}{\nu_0}\right)^{\alpha} + S_{0,\mathrm{s}}\left(\frac{\nu}{\nu_0}\right)^{-0.7} \tag{2.2}$$

where $S_{0,s}$ is the synchrotron component of the flux density at ν_0 and the only free parameter in this fit. Examples of pixel locations fit with a free-free turnover and with a synchrotron component are shown in Figure 2.1. Although frequency-interpolation is performed at each pixel independently, point-to-point scatter is not introduced during this process. This is due to the coherence in intensity of neighboring pixels which have been smoothed over by a Gaussian beam that is 235 square pixels in area.

The short-spacing map frequency-interpolated to 142 MHz is shown in Figure 2.2,*center* for the region of sky falling within the 20% power of the LOFAR primary beam of the observation. We compare the frequency-interpolated short-spacing map at 142 MHz to an all-sky map at 150 MHz with 5° resolution (Landecker & Wielebinski 1970). The survey data in this region of the sky were originally observed at 178 MHz with $5^\circ \times 1.25^\circ$ resolution (Turtle & Baldwin 1962) and then scaled to 150 MHz with a spectral index[3] of $\beta = -2.6$. Since, the survey data have been re-calibrated to attain an 8 K zero level calibration and a scaling error of 1% (Patra et al. 2015). We take a cutout from the survey data which covers our region of interest and convert the intensity units from temperature brightness to Jy beam^{-1}. We convolve our short-spacing map to 5° resolution and re-grid it to match the 0.23° pixel scale. Taking the intensity ratio of the 150 MHz survey image over the convolved short-spacing map at

[2] $S(\nu) = S_0(\nu/\nu_0)^\alpha$
[3] $T_b \propto \nu^\beta$

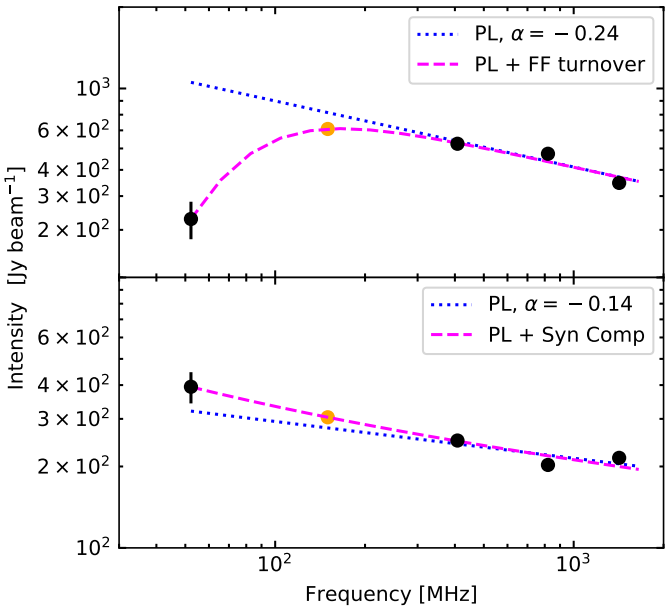

Figure 2.1: Examples of the multi-frequency fits (done on a pixel by pixel basis) to frequency-interpolate the "short-spacing" map – a low resolution image with sensitivity to large angular scales – at 142 MHz. The black data points represent the survey data used in the fit. The orange data point represents the interpolated value at 142 MHz. The dotted blue line represents the power-law fit to the high-frequency data points at 408, 820, and 1420 MHz. The dashed magenta line represents the final SED fit – where either a free-free turnover (*top*) is fit (Equation 2.1) or a synchrotron component (*bottom*) is added (Equation 2.2) to match the low-frequency point at 52 MHz.

142 MHz results in intensity ratios that have a median value of 1.25. This is within sensible agreement as a 25% error falls within the uncertainty of our survey data.

Imaging

The final step in processing the LOFAR observations is imaging the data. We use the frequency-interpolated short-spacing map (Section 2.2.1) as a starting model during imaging in order to deconvolve the interferometric data with zero-level and total flux density information.

To prepare a template for the short-spacing map for `wsclean` (Offringa et al. 2014), we first run `wsclean` with the image weight settings (see below) and 1 iteration so that the pixel grid and synthesized beam size are set. Next we convert the short-spacing map into intensity units of Jy pixel^{-1}according to the synthesized beam size of the `wsclean` image. This is done with the following routine. We re-grid the short-spacing map to match the `wsclean` output pixel grid and size of 18″. Then we scale its intensity by the ratio of the beam areas, ($A_{\texttt{wsclean}}/A_{ss}$), to convert units to Jy beam^{-1}with respect to the `wsclean` output synthesized beam. Next we convert the intensity to units of Jy pixel^{-1} by dividing by the beam area in units of pixels. At this point the short-spacing model is prepared for `wsclean` in true-sky flux density units. `wsclean` requires that we input two model images: one which is attenuated by the primary beam and one which is not. Therefore, we create a copy of our short-spacing model image, but we also apply the primary beam response. We set the primary beam model to zero outside of the first null as we do not image beyond that. With these steps[4], the short-spacing map is prepared to be input to `wsclean`.

We run `wsclean` using the `-predict` option to predict the short-spacing model image into the MODEL column of the measurement set. We then run `wsclean` a second time, now with the `-continue` option to deconvolve the interferometric data. We image out to the first null of the primary beam over an area of $10^\circ \times 10^\circ$. We use Briggs image weighting with a robust parameter of -0.5 and a circular Gaussian taper of $1.5'$, effectively smoothing out the long baselines. We CLEAN with multi-scale cleaning (Offringa & Smirnov 2017) on pixel scales of [0,18,36,72,144] and to a threshold of 4σ where σ is scale dependent and internally calculated.

In Figure 2.2*right*, we show the output short-spacing corrected image. In this paper, we analyze a $4^\circ \times 4^\circ$ region covered by the LOFAR observations, which approximately encompasses the full-width half power of the primary beam. We smoothed the image to a circular beam of FWHM of $2'$. The final image has a noise of 25 mJy beam^{-1} and effective frequency of 142.19 MHz.

For comparison, we also image the LOFAR data without the short-spacing map but using the same imaging parameters and show the results in Figure 2.2*left*. Additionally, we checked our imaging results by convolving the final image to the $72'$ resolution of the initial short-spacing map and verified that the total integrated fluxes are consistent. Lastly, we compare our imaging results by "feathering" (Stanimirovic 2002; Cotton 2017) the short-spacing map with the LOFAR data imaged without

[4]We also verify our template preparation procedure with the CASA preparation procedure outlined by J. Kauffmann at `https://sites.google.com/site/jenskauffmann/research-notes/adding-zero-spa` .

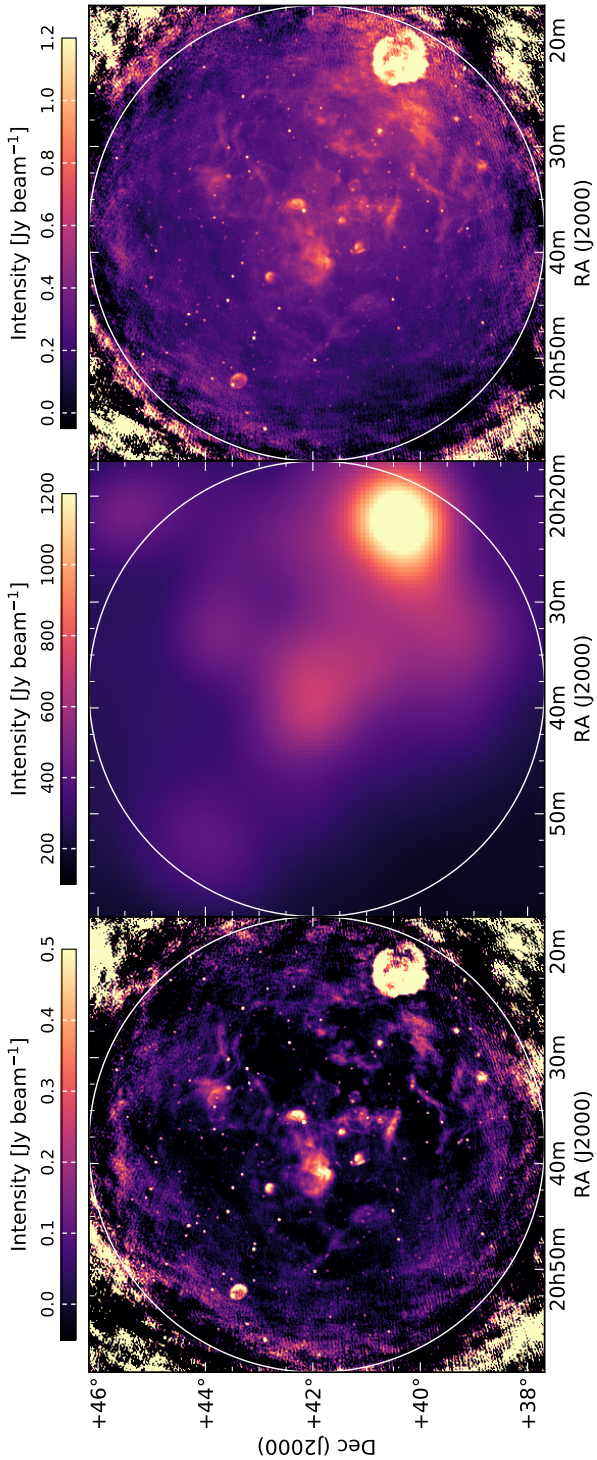

Figure 2.2: Imaging LOFAR 142 MHz observations of the Cygnus X region. The white circle shows the 20% power of the primary beam. We draw attention to the different intensity scales among the images. For reference, Cygnus A is located about 7.4° due west from the center of the pointing. *Left:* Deconvolved LOFAR image without short-spacing information. While these data are sensitive to emission on angular scales as large as 96′, negative (un-physical) emission is present induced by large scale emission in the Galactic plane. *Center:* The frequency-interpolated short-spacing map at 142 MHz (see Section 2.2.1) and 72′ resolution. *Right:* LOFAR data imaged with the short-spacing map as an initial model (see Section 2.2.1).

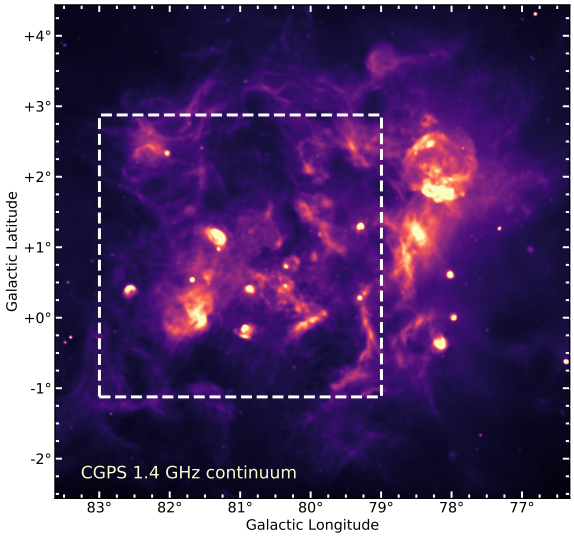

Figure 2.3: The full Cygnus X star-forming region shown in CGPS 1.4 GHz continuum intensity (Taylor et al. 2003). The white dashed lines encompass the region of interest ($4^\circ \times 4^\circ$, or $\sim$100 pc $\times$ 100 pc) that we analyze with LOFAR 142 MHz observations.

short-spacings. Through feathering, images are combined in the domain of their Fourier transforms by a weighted average in order to extract the most appropriate spatial frequencies from each image. Taking the intensity ratio of the `CASAfeather` and the `wsclean` created images, we find a mean and median value of 1.06 computed over the $4^\circ \times 4^\circ$ region.

2.2.2 Ancillary Data

We compare the LOFAR data with observations compiled through the Canadian Galactic Plane Survey (CGPS; Taylor et al. 2003) at 1420 MHz. These data were observed with the Synthesis Telescope at the Dominion Radio Astrophysical Observatory with short-spacing corrections, in this region, using the Stockert 25 m survey (Reich 1982). Since the effective resolution varies across the mosaic data products – the synthesized beam is declination dependent – we processed the mosaics to attain a common resolution of $2'$. Then we stitch the smoothed mosaics together. The standard deviation in a relatively low emission region of the image is $\sigma = 0.03$ K (0.7 mJy beam^{-1}).

2.3 Continuum Emission

The Cygnus X star-forming complex encompasses an area of more than 50 square degrees as shown in Figure 2.3. The region of interest analyzed with our LOFAR pointing, $4^\circ \times 4^\circ$ (100 pc $\times$ 100 pc) is depicted with white dashed lines.

Figure 2.4 shows the continuum emission observed at 142 MHz with LOFAR and which is corrected for missing short-baseline information (Section 2.2.1). The 142 MHz emission in this region primarily traces thermal free-free emission from ionized gas with low density and small emission measure (see Section 2.4 and e.g., Wendker et al. 1991). Thermal radiation referred to as "free-free" emission is bremsstrahlung radiation emitted as the paths of free electrons are deflected in the presence of free ions.

The morphology of the 142 MHz emission includes extended (on degrees scales), resolved regions of photoionized gas in the vicinity of massive stars and star clusters. Filaments are a prominent feature in bright and also faint emission regions. Shell-like regions also appear. An additional diffuse component surrounds much of the extended structures. Extra-galactic radio galaxies with bright synchrotron emission at these frequencies appear as point-like sources. Analyzing the spectral energy distribution (SED; see Section 2.4) of unresolved objects is necessary to pull-out synchrotron dominated sources from the regions of active star-formation embedded within a dense medium.

The locations of massive stars and star clusters are shown in Figure 2.5. We label the radio continuum features which were identified in Downes & Rinehart (1966) with 4.8 GHz observations – DR 7, 10, 11, 16, 18, 19, 20, 21, 22, 23. Only DR 7 is not associated with the Cygnus X region; instead it is located more than 3.3 kpc distant in the Perseus Arm. The Cygnus X region has been extensively surveyed for massive stars and clusters (Comerón & Pasquali 2012; Wright et al. 2015; Berlanas et al. 2018; Comerón et al. 2020). Confirmed OB stars within the Cyg OB2 association and in the field are marked by small green stars (Berlanas et al. 2018) and blue stars mark massive supergiants (Comerón et al. 2020). Large green stars mark candidate star clusters (Le Duigou & Knodlseder 2002).

The 1.4 GHz continuum emission from the CGPS, also shown in Figure 2.5, is strikingly similar to the LOFAR 142 MHz continuum emission. The morphologies and relative intensities of the extended, resolved emission (including filaments) are comparable. Even regions which are devoid of emission seem to agree. The low-level, diffuse emission surrounding extended structures is relatively brighter at lower frequencies. Similarities attest to the primarily thermal nature of the emission (Xu et al. 2013; Wendker et al. 1991). Differences in relative intensities arise in compact sources and are attributed to two effects. One, compact regions which appear relatively fainter at 142 MHz have high emission measures ($EM > 10^6$ pc cm^{-6}) and large optical depths ($\tau_{\rm ff} > 10$). Two, at 1.4 GHz the synchrotron emission from extra-galactic sources is faint compared with the thermal component from galactic regions.

Mid-infrared (MIR) emission at 3.6, 8.0, and 24 μm is compiled as an RGB image in Figure 2.5. Emission at 3.6 μm in blue and observed with the *Spitzer* Space Telescope[5] shows the stellar population of young massive stars as point-like sources of emission (Beerer et al. 2010). 8 μm emission observed with the Midcourse Space Experiment (MSX; Price et al. 2001) and described by Schneider et al. (2006) especially with respect to CO, mainly traces UV heated polycyclic aromatic hydrocarbons

[5] *Spitzer* data was acquired from the archive at `https://irsa.ipac.caltech.edu/data/SPITZER/Cygnus-X/` .

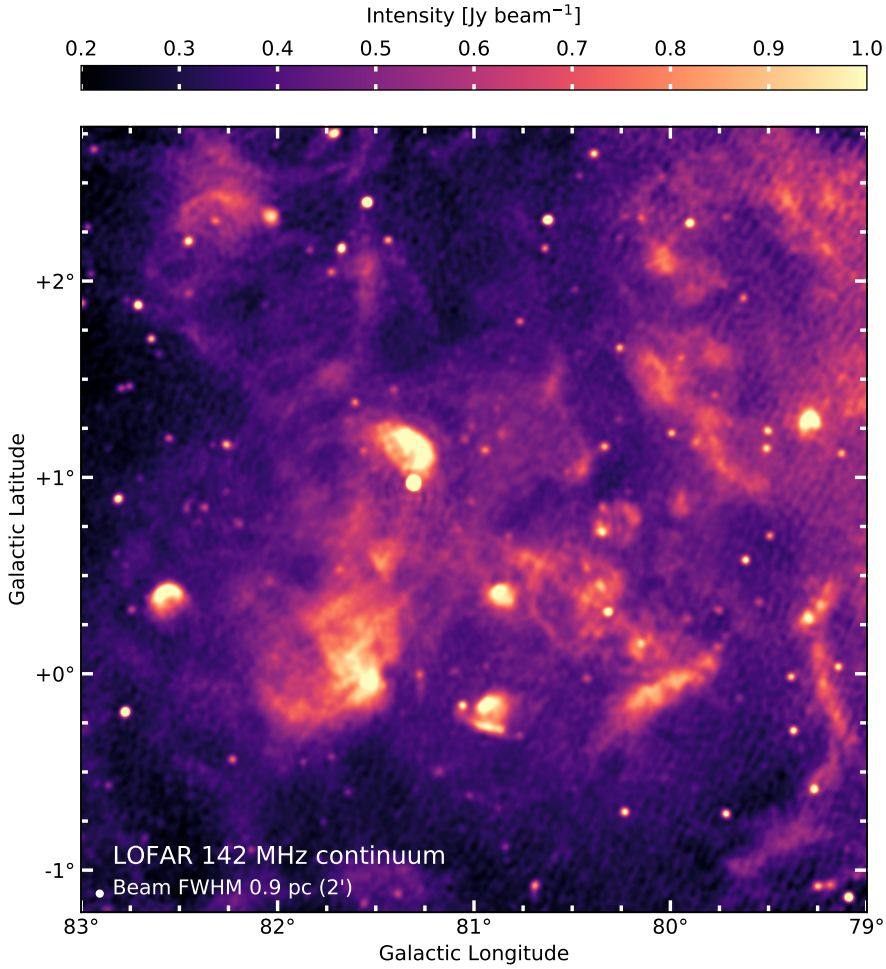

Figure 2.4: LOFAR 142 MHz continuum emission of the 4° × 4° (∼100 pc × 100 pc) area in the Cygnus X region that we analyze at 2′ (0.9 pc) resolution. The emission in this region is primarily thermal, free-free emission from low-density photoionized gas. A number of extra-galactic radio sources are present as bright, point sources. The noise away from bright emission is σ = 25 mJy beam^{-1}.

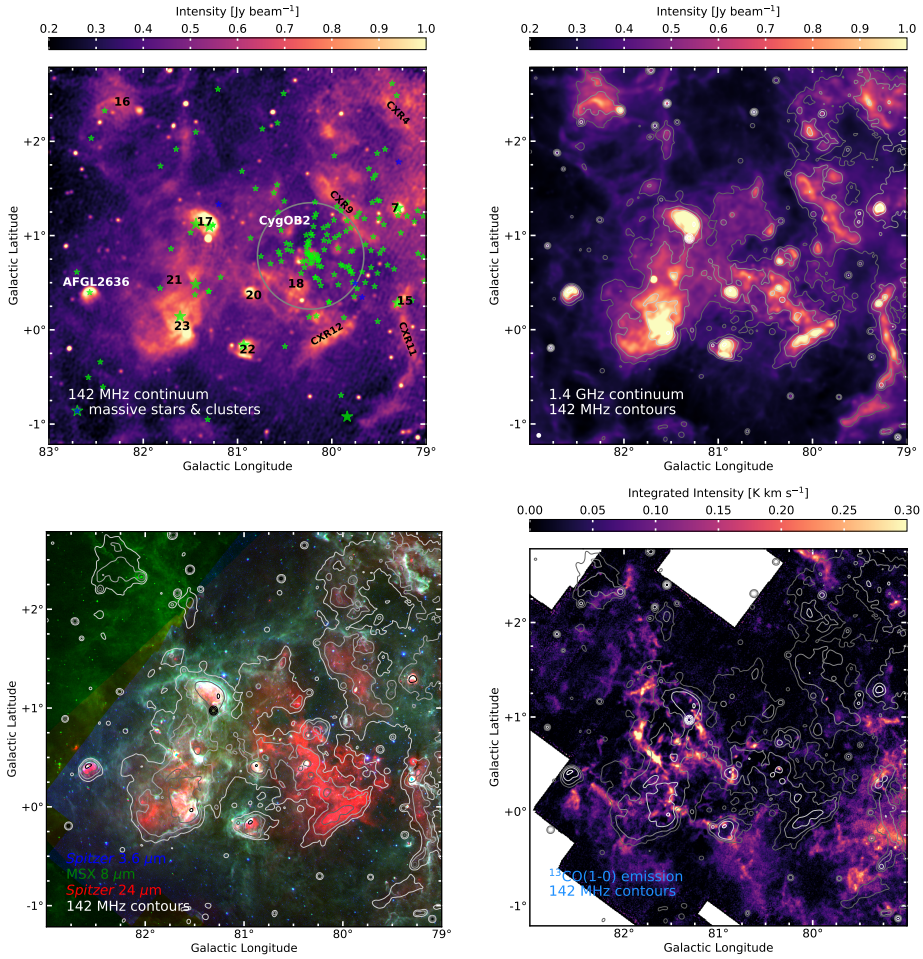

Figure 2.5: *Top Left:* The location of massive stars and star clusters are shown overlaid on LOFAR 142 MHz continuum emission. Small green stars represent massive OB stars of the Cyg OB2 association and within the field (Berlanas et al. 2018), and small blue stars mark the locations of supergiants (Comerón et al. 2020). The gray circle represents the core of Cyg OB2 as identified by Wright et al. (2015). Large green stars mark the location of (open) clusters in the region (Le Duigou & Knodlseder 2002). Additionally, numbers in black denote the position of radio continuum sources as identified by Downes & Rinehart (1966). Filaments identified by Wendker et al. (1991) are designated with "CXR". *Top Right:* 1.4 GHz continuum emission observed through the CGPS (Taylor et al. 2003) and smoothed to a common resolution of $2'$. Contours from the LOFAR 142 MHz continuum are overlaid at $0.3 + [3, 3\sqrt{3}, 9, ...]\sigma$ where $\sigma = 0.05$ Jy beam^{-1}. The morphology in the majority of extended features in strikingly similar between 142 GHz and 1.4 GHz, consistent with thermal continuum from low-density, ionized gas; however, optical depth effects present in bright extended regions become apparent as the relative intensity of the emission is brighter at 1.4 GHz (deviating from the $S \propto \nu^{-0.12}$ dependence of optically thin emission). High-density regions such as DR 21 are brighter in 1.4 GHz emission, whereas the point-like sources which are dominated by synchrotron emission, primarily of extra-galactic background galaxies, are fainter in 1.4 GHz emission. *Bottom Left:* MIR emission. In blue, *Spitzer* 3.6 μm tracing the stellar population. In green, MSX 8 μm emission primarily from PAHs heated by UV radiation from massive stars tracing the PDR surfaces. In red, *Spitzer* 24 μm emission of warm dust, corresponding well with diffuse ionized gas observed at 142 MHz. *Bottom Right:*. ^{13}CO (1-0) integrated intensity observed with FCRAO (Schneider et al. 2011) tracing the bulk of the molecular gas.

(PAHs) in photodissociation regions (PDRs), thereby emphasizing interfaces between molecular clouds and intense UV fields from young massive stars. *Spitzer* 24 μm emission is predominantly produced by thermal emission from warm dust co-spatial with photoioinized gas (Churchwell et al. 2006; Calzetti et al. 2007; Salgado et al. 2012). Bright 24 μm emission in red corresponds well with the ionized gas traced by low-frequency radio emission. A correspondence is present for H II regions (partially) surrounded by PDR envelopes as well as for ionized regions without higher density PDRs at their edges.

Molecular cloud emission as traced by ^{13}CO(1-0) (Schneider et al. 2011) shows the cold gaseous reservoir with respect to massive stars in Figure 2.5. The full Cygnus X complex (see Figure 2.3) contains 4.7×10^6 M$_\odot$ of molecular gas with an average density of $\sim$60 cm^{-3} (Schneider et al. 2006). High-contrast elongated filaments are observed as well as diffuse emission from higher density clouds. Embedded regions like DR 21, DR 15 and DR 20 are sites of active star-formation coincident with radio emission, whereas DR 17, DR 18, DR 22, and DR 23 are located at the edges of or well-separated from molecular clouds. Several arc or shell-like structures are also visible in CO.

2.4 Mapping the physical properties of ionized gas

The observed intensity of optically thin, free-free emission is a function of frequency (e.g., Condon 1992; Emig et al. 2020b),

$$I_{\rm ff}(\nu) = \left(1.034 \times 10^5 \text{ Jy beam}^{-1}\right) \left(\frac{A}{\rm sr}\right)^{-1} \left(\frac{EM_+}{10^3 \text{ cm}^{-6} \text{ pc}}\right) \left(\frac{T_e}{10^4 \text{ K}}\right)^{-0.323} \times \left(\frac{\nu}{\rm GHz}\right)^{-0.118} \tag{2.3}$$

and which we express as being dependent on the area of the beam in steradians, A, the electron temperature, T_e, and the emission measure, EM_+, of the ionized medium. The emission measure,

$$EM_+ = \int n_e n_+ {\rm d}l \tag{2.4}$$

is defined by the electron density, n_e, by the ion density, n_+, and by the pathlength integral of the emitting region. Fitting the free-free SED at frequencies where the radiation becomes optically thick and will thus be self-absorbed — such that the optical depth, $\tau_{\rm ff}$, is given by (Condon 1992; Emig et al. 2020b),

$$\tau_{\rm ff}(\nu) = 3.37 \times 10^{-4} \left(\frac{EM_+}{10^3 \text{ cm}^{-6} \text{ pc}}\right) \left(\frac{T_e}{10^4 \text{ K}}\right)^{-1.323} \left(\frac{\nu}{1 \text{ GHz}}\right)^{-2.118} \tag{2.5}$$

— allows for the electron temperature and emission measure to be determined.

In this section we use the LOFAR image to map out the physical properties of the free-free emitting gas in order to better understand the influence of ionized gas (e.g., through gas pressure) and how its ionization is maintained. We fit for the optical depth at 142 MHz (Figure 2.6). From the free-free turnover and SED, we derive the emission measure (Figure 2.7).

2.4.1 Fitting the free-free optical depth at 142 MHz

The radio emission arising from the extended, resolved features in the Cygnus X region is consistent with optically thin thermal, free-free emission at frequencies as low as 408 MHz (Wendker et al. 1991; Xu et al. 2013). A dominating component of thermal emission is further supported by the relative intensities between the 142 MHz and 1.4 GHz image, as discussed in Section 2.3. Therefore, fitting the regions of emission as single components between 1.4 GHz and 142 MHz is a reasonable assumption.

We fit for the optical depth at 142 MHz using the LOFAR data, the 1.4 GHz CGPS data, and the expected frequency dependence of free-free emission. We first prepare the CGPS data for processing by regridding the image to the same pixel grid as the LOFAR image. We use a similar procedure to fit the SED as described in Section 2.2.1. For each pixel, we use the 1.4 GHz data point as the anchoring intensity measurement. Assuming the intensity is thermal and optically thin, we extrapolate it to 142 MHz. If the intensity at 142 MHz is less than the extrapolated value, we fit for a free-free turnover as in Equation 2.1. Otherwise, if the intensity at 142 MHz is greater than the extrapolated value, we assign $\tau = 0$ for that pixel. An example of the free-free fitting process is shown in Figure 2.1. The error of the optical depth is determined from the formal fit errors.

Maps of the free-free optical depth at 142 MHz and its error are shown in Figure 2.6. We find measurable optical depths ($\tau > 0.01$) in a large portion (77% of pixels) of the image. The extended resolved structures have optical depths up to $\tau_{\rm ff} = 1.5$. The largest optical depths are found in the compact sources exceeding $\tau_{\rm ff} > 5$. In the densest regions of AFGL 2637, DR 15, DR 21, and DR 22, optical depth effects are already important (e.g., $\tau > 0.1$) at 1.4 GHz (Wendker et al. 1991); since their intensity at 1.4 GHz is not consistent with the optically thin assumption, the values we determine here underestimate their true optical depths at 142 MHz.

Shallower sensitives and imperfections in the beam model towards the image outskirts result in less reliable intensities and thus optical depths determined there. However, the comparison between our final image and that obtained by feathering (Section 2.2.1) indicate that our results are reliable towards all resolved (DR) sources and in the diffuse emission within $\sim$1.5° from the center of the pointing.

2.4.2 Mapping the free-free emission measure

From the estimated optical depth, we use Equation 2.5 to derive maps of the free-free emission measure. At each pixel, we take the optical depth value, set $T_e = 7400$ K and $\nu = 142$ MHz, and solve for the EM. The results are shown in Figure 2.7. A temperature of $T_e = 7400$ K is the median temperature derived from radio recombination line observations at 4.8 GHz and 2.6′ resolution (Piepenbrink & Wendker 1988) and is consistent with the value of $T_e \approx 7500$ K derived in the DR 21 region with 2.5″ resolution observations (Harris 1973). At 2′ resolution, we find emission measures ranging from $EM_{\rm ff} = (2-40) \times 10^3$ pc cm^{-6} in the extended features, and in compact unresolved sources, $EM_{\rm ff} = 4 \times 10^4$ pc cm^{-6} to $EM_{\rm ff} \leq 3 \times 10^5$ pc cm^{-6}.

From Equation 2.5, we have that at 1.4 GHz a free-free optical depth of $\tau_{\rm ff} = 0.1$ (1) corresponds to $EM = 4 \times 10^5$ (10^6) pc cm^{-6}. Thus we expect to measure an upper limit of $EM \lesssim 4 \times 10^5$ pc cm^{-6}. Regions with $EM \gtrsim 4 \times 10^5$ tend to be compact,

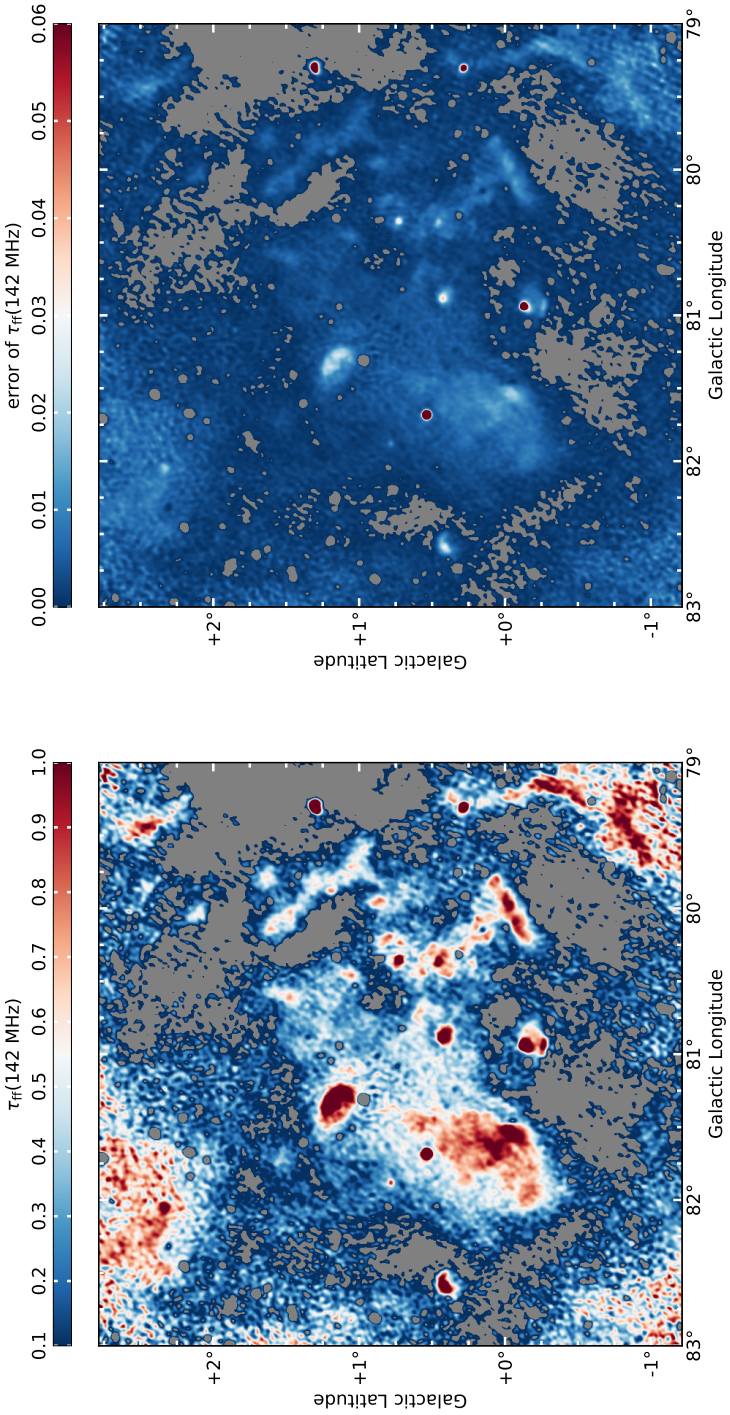

Figure 2.6: The free-free optical depth, $\tau_{\rm ff}$, at 142 MHz. Regions which are optically thick ($\tau_{\rm ff} > 1$) are dark red. Pixels for which a free-free turnover was not fit are shown in gray. Extra-galactic radio galaxies, dominated by synchrotron emission, are present in the region as unresolved point-like sources (in gray) with negligible free-free optical depths. *Right:* The error map of the fitted optical depth at 142 MHz. The error on the optical depth is typically 10%.

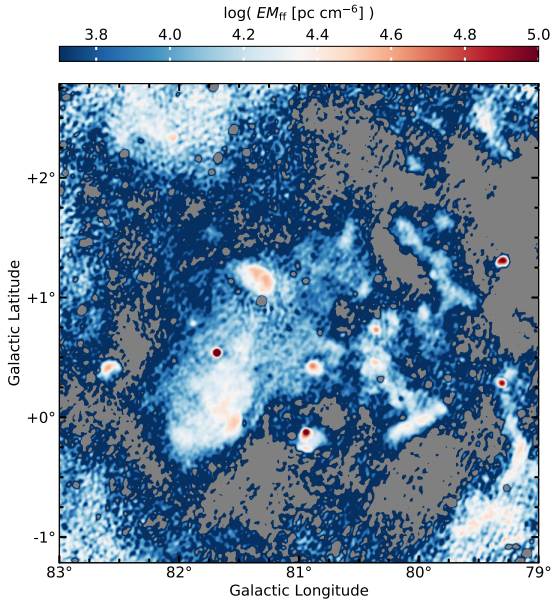

Figure 2.7: Free-free emission measure, $EM_{\rm ff}$, shown in log stretch, of photoionized gas. Tests of the imaging process (Section 2.2.1) find that our results are reliable towards all DR sources and in the diffuse emission within $\sim$1.5° from the center of the pointing. Shallower sensitives and an imperfect beam model towards the image outskirts result in less robust estimates.

dense regions where massive stars have yet to shed their natal material. For example, regions of $\sim$1 pc would have electron densities of $n_e \gtrsim 600$ cm^{-3} at this emission measure limit. Following the same procedure for the lower limit, we have that at 142 MHz a free-free optical depth of $\tau_{\rm ff} = 0.1$ corresponds to $EM = 3 \times 10^3$ pc cm^{-6}. These limits are consistent with what we derive.

The emission measures we map out are consistent with previous lower resolution findings (Downes & Rinehart 1966) and previous estimates of individual regions (Wendker et al. 1991). However, with the higher resolution of our analysis, we do see spatial variations of the emission measure which span a larger range of EM values. These emission measures also agree well with the emission measures derived from optically thin 1.4 GHz continuum. As the sensitivity of the CGPS 1.4 GHz data is significantly deeper for the current bandwidth of LOFAR data employed, we use the CGPS data in the remainder of this analysis.

2.5 Analyzing filaments

Filamentary structure is a prominent feature of the low-density ($n_e \lesssim 100$ cm^{-3}) ionized gas in the Cygnus X region, as we point out in Section 2.3 and which is also seen over a larger area of the Cygnus X region in Figure 2.3. We are motivated to derive properties of these filaments to investigate how ionizing radiation interacts

with and shapes its environment. To briefly summarize the contents of this section, Figure 2.8 shows the 906 filaments identified with the `DisPerSE` algorithm (Sousbie 2011). Figure 2.9 demonstrates the processing and fitting of the radial distribution of a filament profile using `FilChaP` (Suri et al. 2019). We plot the distributions of the peak EM fit to the radial profiles, the best-fit widths, and the inferred electron densities in Figure 2.10. The peak EMs of the filament profiles follow a power law in their number distribution down to the estimated completeness limit. The widths of the filament profiles show a characteristic peak at a median value of 3.6 pc (noting that our beam resolution is 0.9 pc). The median electron density within filaments is $n_e = 38$ cm^{-3}, with densities spanning $n_e = 10 - 500$ cm^{-3}. Figure 2.11 and 2.12 compile and compare the peak EM, width and density.

2.5.1 Identifying filaments

Using the Discrete Persistent Structures Extractor (`DisPerSE`; Sousbie 2011), we identify 906 filaments in the Cygnus X Region as shown in Figure 2.8. `DisPerSE` uses discrete Morse theory to derive information on the topology of a given data set. Filaments are identified as the set of arcs joining maxima and saddle points. Persistence theory is used to filter out and identify filaments with significance. We refer the reader to Sousbie (2011) for a detailed description of the procedures. `DisPerSE` has been widely used to extract filamentary structures both in observational and simulated datasets (e.g., André et al. 2014, and references therein).

We apply the `DisPerSE` algorithm to a map of the emission measure derived from the CGPS 1.4 GHz intensity using Equation 2.3. We filter the filament identification output of `DisPerSE` using the `-breakdown` option to merge overlapping filament segments and with `-trimBelow` to remove arcs below a robust persistence[6] of 5300 pc cm^{-6}. The rms in low intensity regions of the EM map, interpreted as the offset value or background contribution, is 5300 pc cm^{-6} and the standard deviation, interpreted as the noise, is $\sigma \approx 53$ pc cm^{-6}. Our input parameters to `DisPerSE` result in local maximum and saddle point peak EM intensities of $\gtrsim 9500$ pc cm^{-6} being identified. Filaments are output as lists of image coordinates sampled with points at each half pixel shift in direction.

2.5.2 Fitting filament profiles

We characterize properties of filaments using the python-based Filament Characterization Package (`FilChaP`; Suri et al. 2019) which was designed to work together with `DisPerSE`. Here we give a brief explanation of the procedures implemented in `FilChaP` and refer the reader to Suri et al. (2019) for more detailed descriptions. `FilChaP` takes as input a list of filament coordinates. At each sample point along the filament, a radial profile perpendicular to the filament spine is extracted. The radial profile extends to ± 130 pixels, which we choose so that a baseline estimate includes true background emission at any location in the image.[7] The radial profiles extracted

[6] for the specific implementation see `http://www2.iap.fr/users/sousbie/web/html/index959e.html?post/definitions`

[7] We padded the image with true EM intensity so that filament profiles at edges of the region would be fully sampled.

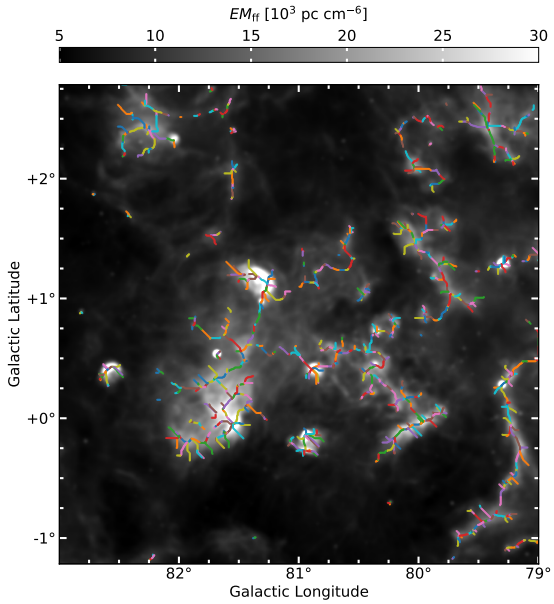

Figure 2.8: The 906 filaments identified with `DisPerSE`. Each filament is displayed in a different (arbitrary) color. The grayscale image is the emission measure, computed from the 1.4 GHz continuum intensity assuming optically thin thermal emission, and is the image on which the filaments are identified.

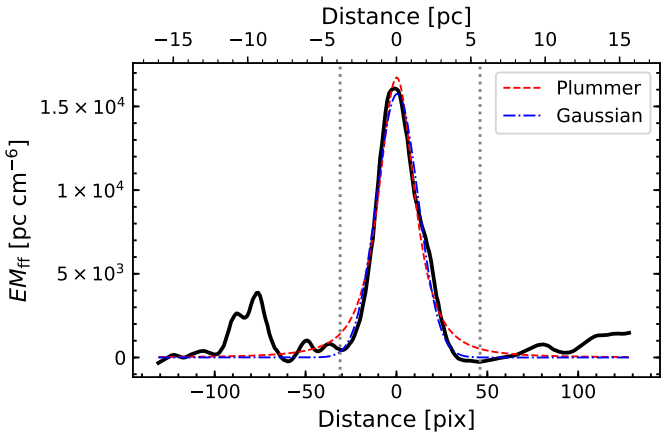

Figure 2.9: An *EM* radial profile of a filament segment, shown with a black solid line. The radial profile has been baseline (and background) subtracted. Negative distances from the spine point to the northeast direction, and positive distances to southwest of the filament. The red, dashed line is the best fit Plummer, $p = 4$ profile used to compute the filament profile properties. The blue dot-dashed line shows the best fit Gaussian for comparison.

at four consecutive sample points of the filament are averaged together. This mean radial profile is baseline subtracted, effectively removing any background emission and baseline gradient. To the mean radial profile, `FilChaP` fits three line profiles — a Gaussian and two Plummer profiles — and computes the second moment[8] width. We demonstrate a radial profile processed and fit with `FilChaP` in Figure 2.9.

Plummer-like functions have been used to describe the column density of a filament with a dense and flat inner portion and a power-law decline at larger radii (e.g., Arzoumanian et al. 2011):

$$\Sigma_p(r) = A_p \frac{\rho_c R_{\rm flat}}{\left[1 + \left(\frac{r}{R_{\rm flat}}\right)\right]^{\left(\frac{p-1}{2}\right)}} \tag{2.6}$$

where ρ_c is the critical density, $R_{\rm flat}$ is the radius within which the density is uniform, p is the power law index, and A_p is a finite constant that is related to the filament's inclination compared to the plane of the sky (here we assume that this angle is zero). Two literature values of the index are fit in `FilChaP`, $p = 4$ for the density of a homogeneous isothermal cylinder (Ostriker 1964) and $p = 2$ as the value derived from embedded star-forming filaments identified with *Herschel* observations (Arzoumanian et al. 2011).

The filament properties that we report are consistent with the four different types of fits and determinations – as we show in Appendix 2.A. Since a Plummer profile with $p = 4$ results in a slightly lower reduced chi-squared, we use the properties derived from this fit to represent our results. Through the line fitting process, 2073 mean radial profiles are constructed. We remove poor fits, with widths less than 3 pixels, resulting in 1934 filament profiles that we analyze.

2.5.3 Filament properties

Peak EM of filaments

We determine the peak of the EM radial profile (which has been background and baseline subtracted) from the best fit of a Plummer $p = 4$ line profile to 1934 mean radial profiles extracted within 906 filaments. In Figure 2.10, we plot a histogram of the peak EMs. We find peak EMs ranging from 500 pc cm^{-6} to 10^5 pc cm^{-6}, with a median value of 5.5×10^3 pc cm^{-6}.

We discuss the completeness of the distribution. We previously mention, in Section 2.4.2, the upper limit to our EM sensitivity of 4×10^5 pc cm^{-6}. Since the rms in low intensity regions is equal to 5.3×10^3 pc cm^{-6}, we expect an upper bound to fully sampled emission measures of $< 3.5 \times 10^5$ pc cm^{-6}. Furthermore, we applied a cut to select filaments with a peak $EM > 9.5 \times 10^3$ pc cm^{-6}. Subtracting the "background" EM, which will be greater than or equal to 5.3×10^3 pc cm^{-6}, results in an estimated completeness of 4.2×10^3 pc cm^{-6}. Therefore, filaments with a fitted peak EM below 4.2×10^3 pc cm^{-6} are not fully sampled.

[8]The nth moment of a distribution I is given by, $m_n = (N\sigma^n)^{-1}\Sigma_i^N I_i(x_i - \bar{x})^n$, where $\bar{x}$ is the intensity weighted mean position of the profile, I_i is the intensity at position x_i, and σ is the intensity weighted standard deviation of the profile.

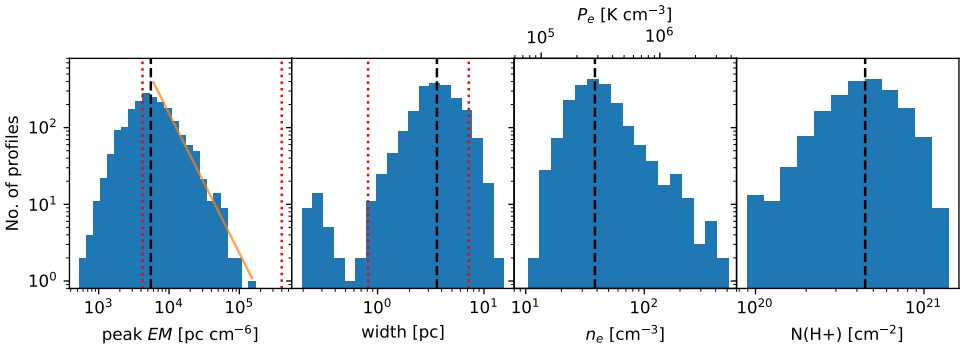

Figure 2.10: Histograms of filament properties inferred from fits to their EM radial profiles. We fit a Plummer, $p = 4$ line profile to the radial distributions. Black dashed lines mark the median values. Red dotted lines mark the estimated completeness limits in the EM and width plots. *Left:* Peak emission measure (EM) of the best fit in units of pc cm^{-6}. The median EM of the filaments identified in this analysis is 5530 pc cm^{-6}. The orange solid line shows the power-law, $\beta = -1.8 \pm 0.1$, fit to the distribution for $EM > 5530$ pc cm^{-6}. *Center left:* Filament FWHM in units of pc. The median FWHM of the filaments identified in this analysis is 3.6 pc. The resolution of the beam FWHM ($2'$, 0.9 pc) is marked (with a red dotted line) as the lower completeness limit. Widths smaller than the beam resolution result from poor fits. *Center right:* Average electron density of the filament profiles in units of cm^{-3}, computed with the best fit peak EM and width as $n_e = \sqrt{EM/\ell}$ where ℓ is the FWHM of the Plummer profile. The median electron density of the filaments identified in this analysis is 38 cm^{-3}. The electron pressure, computed as $P_e/k_{\rm B} \sim 7400$ K $\cdot\, n_e$, is shown along the top axis. *Right:* The column density of ionized hydrogen, letting $n_e \sim n_{\rm H^+}$.

We fit a power-law to the number distribution of the peak EM for bins which we consider to be complete. This results in a best fit power-law index of $\beta = -1.8 \pm 0.1$.

Filament widths

We determine the widths from the Plummer $p = 4$ fits to the mean radial profiles of the filaments. The FWHM of a Plummer $p = 4$ profile is FWHM $= 1.533 \cdot R_{\rm flat}$, see Equation 2.6 for $R_{\rm flat}$. In Figure 2.10, we plot the best fit FWHM of each mean radial profile, converted into physical units assuming an average distance of $d = 1.5$ kpc to the complex. A peak in the width distribution arises at 3.6 pc, which is well separated from the beam resolution of 0.9 pc ($2'$). We note that widths smaller than the image resolution likely result from poor, unreliable fits and should be interpreted as non-physical. While the `DisPerSE` algorithm does not prevent large scale features from being identified, there are regions of diffuse emission that could possibly be identified as "filaments" at lower resolution. For the EM we probe, we place a conservative upper completeness limit to the filaments widths of 7.2 pc, twice the median value. In Figure 2.11 we show the filament widths with respect to their spatial location on the EM map. Bright compact regions of emission tend to have smaller widths (in blue). Also notable is the DR 23 region which has somewhat wider filaments (in orange/red) than average.

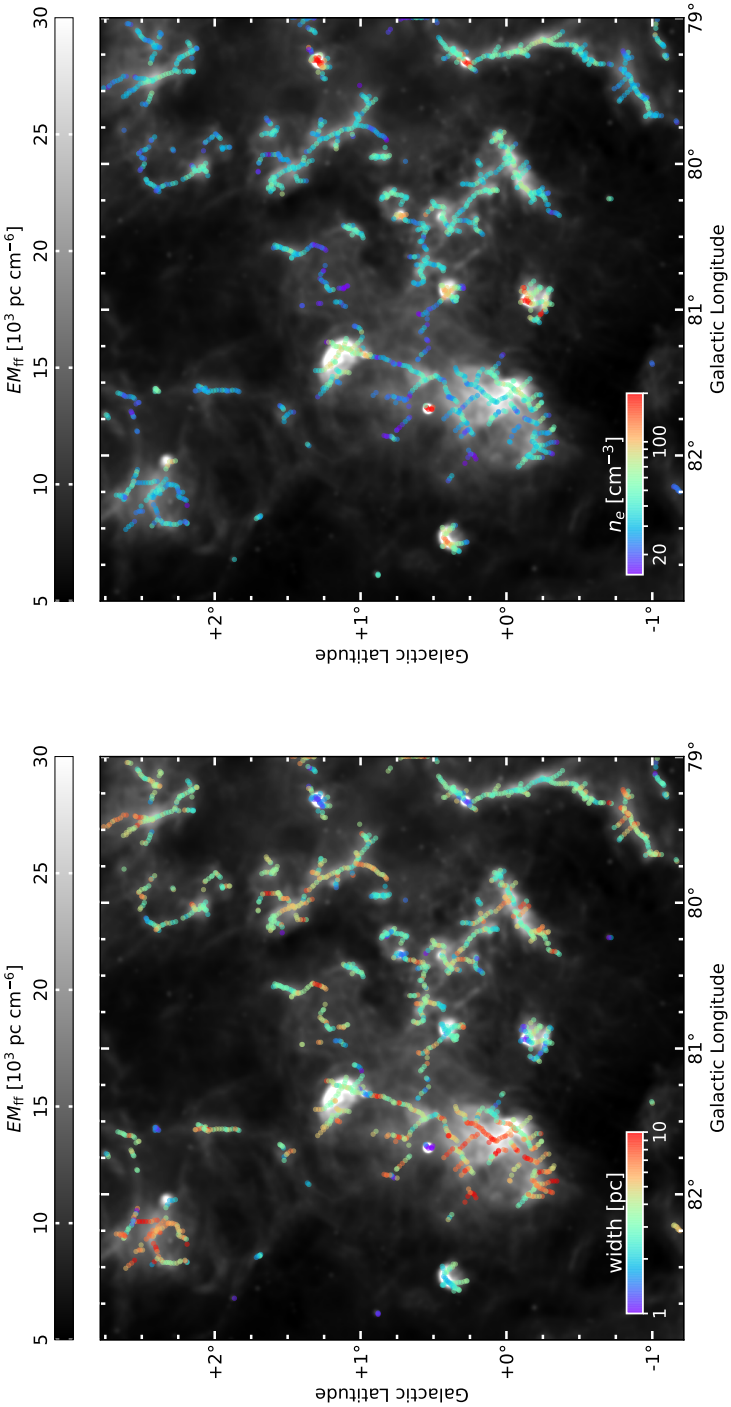

Figure 2.11: *Left:* Width of filaments' mean radial profiles are represented as colored data points and overplotted on the *EM* map. Compact bright regions, tend to have smaller widths. Another notable is the DR 23 region which has wider filaments than average. *Right:* The estimated density of each radial profile are represented as colored data points and overplotted on the *EM* map. As expected, densities are highest in known star-forming regions. Assuming the filaments are fully ionized and have a common temperature of 7400 K, the thermal pressure would be directly proportional to the density, $P_{\rm th}/k_{\rm B} \sim 2 \cdot 7400\ {\rm K} \cdot n_e$.

Electron densities of filaments

We estimate the electron density of the filament from the best fit peak EM and width of the Plummer $p = 4$ line profile, as $n_e = \sqrt{EM/\text{width}}$. In Figure 2.10, we plot the distribution in electron density of the mean radial profiles. Electron densities ranging from 10 cm^{-3} to 500 cm^{-3} are found, with a median value of 38 cm^{-3}. In Figure 2.11 we show the filament densities with respect to their spatial location on the EM map.

From the estimated completeness of emission measure and spatial scales, we estimate our completeness and sensitivity to electron densities. At the lowest possible (background subtracted) emission measure, $EM > 4.2 \times 10^3$ pc cm^{-6}, the upper bound on the width, FWHM < 7.2 pc, puts a hard limit to the possible electron densities, $n_e > 24$ cm^{-3}. Likewise, a hard upper limit to the electron density that we reliably detect, $n_e < 710$ cm^{-3}, arises from the largest possible emission measure, $EM < 4 \times 10^5$ pc cm^{-6} and the smallest width of 0.9 pc. However, our census of electron densities may not be complete for the electron densities within the range $24 < n_e$ [cm^{-3}] < 710.

Column density of ionized gas

From the density and width we compute the column density of ionized gas. We assume the gas is completely ionized, with $n_e \sim n_{\rm H\,II}$, and compute a column density of $N(\text{H II}) = \int n_e \mathrm{d}\ell = \sqrt{EM \cdot \text{width}}$. The ionized hydrogen column densities we derive range from $(10^{20} - 10^{21})$ cm^{-2} with a median value of 4.6×10^{20} cm^{-2}. Based on the estimated completeness of the emission measure and filament width, we can probe column densities in the range of $1.8 \times 10^{20} < N(\text{HII}) < 5.2 \times 10^{21}$. However, given how we derive the column density, we do not expect our census to be complete for any range of column densities.

Pressure of ionized gas

We calculate the electron pressure, as $P_e/k_{\rm B} \sim T_e n_e$, from the ionized gas densities and again assume $T_e = 7400$ K. We find electron pressures of 7.4×10^4 K cm^{-3} to 3.7×10^6 K cm^{-3} with a median value of $P_e/k_{\rm B} \sim 2.8 \times 10^5$ K cm^{-3}. We show these values along the upper axis of the electron density histogram in Figure 2.10. These regions are over-pressured compared with typical values in the diffuse ISM, $P/k_{\rm B} \sim 3.8 \times 10^3$ K cm^{-3} (Jenkins & Tripp 2001; Jenkins et al. 2011). Over-pressure compared to the general ISM is expected for a region where massive stars are interacting with their environment, as massive stars create regions of high pressure that will expand. Indeed the pressures we find do coincide with a small fraction ($\sim$0.05%) of nearly all gas surveyed that has a large pressure ($> 3 \times 10^5$ K cm^{-3}) and which is more prevalent at high velocities or for regions with enhanced starlight densities (Jenkins et al. 2011).

Correlation between filament properties?

In Figure 2.12 we plot the peak EM of the filaments' profiles as a function of the profile width. We color the data points by the inferred electron density. The filament peaks

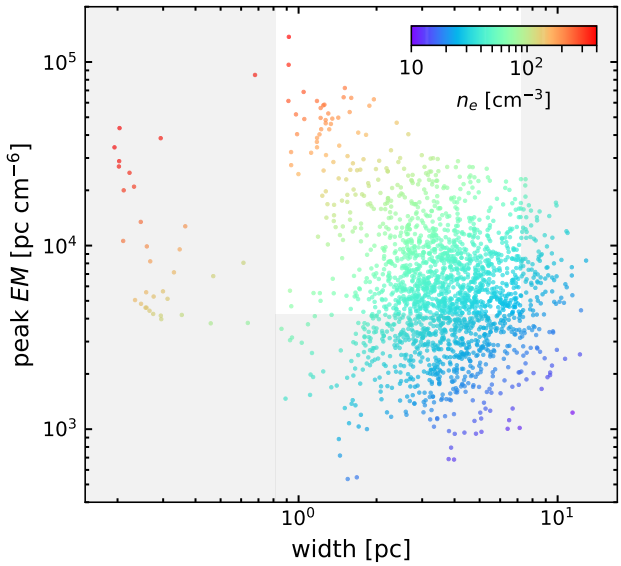

Figure 2.12: Peak EM of the best fit to the filament radial profile plotted with the best fit FWHM. The areas in gray represent values which fall outside of our completeness limits. The colors of the data points represent the electron density inferred from the filament EM and width. Profiles with FWHM smaller than the resolution beam of 0.9 pc likely have poor fits.

and widths do not appear to be correlated. A dearth of high intensity EM filaments with large widths would physically be harder to maintain and may represent a true de-populated portion of this plot.

2.6 Discussion

In this section we discuss the sources which maintain the ionization of the thermally emitting gas that we observe. We find Cyg OB2 may have a considerable influence, ionizing up to two-thirds of the emission in this region. We also discuss what is forming the filaments – likely photoevaporating surfaces of neutral material, flowing into lower-density volume-filling ionized gas. While our calculations suggest that the stellar winds of Cyg OB2 may be dissipating turbulence in the form of transitory filaments, the filament densities correlate with incident radiation and thus suggest only a minority of filaments are influenced by the stellar winds of Cyg OB2. We place our results in the context of ionized gas surveyed with [N II] FIR fine structure lines — finding remarkable agreement with properties — and we construct a framework in this region for ELD ionized gas and how it is maintained. Lastly, we inform on a bright future for LOFAR observations of diffuse emission in the Galactic plane.

2.6.1 Source of ionization of the filaments

The recombination time of warm ionized gas is generally short; $t_{\rm rec} = (\alpha_B n_e)^{-1} \sim$ 2600 yr for gas of density $n_e = 38$ cm^{-3} and temperature $T_e = 7400$ K. Thus an active source of ionizing radiation is required to maintain it. In this subsection, we describe what sources ionize the low-density gas that we observe. We ultimately find that the ionizing radiation from Cyg OB2 (Figure 2.13) can be responsible for up to two-thirds of the total ionized emission in the region, and similarly, two-thirds of ionized emission in filamentary structure. The remaining one-third of emission requires a local source of ionizing radiation, from active regions of star formation or massive field stars. Filaments that we attribute to be (externally) influenced by Cyg OB2 (e.g., see Figure 2.14 and Table 2.1) contrast with the conclusions reached by Wendker et al. (1991) that the filaments result from strings of intrinsic B stars. A general conclusion from this section is thus that massive OB stars which are no longer locally confined by dense gas play a prominent role in shaping filamentary structure of ionized gas.

Local massive stars

Signatures of the youngest, most dense regions of active star formation are not traced at these frequencies and resolution (e.g. DR 15, DR 21, and W75N). Somewhat more evolved regions which have begun bursting open have lower density and smaller emission measures, as we see, leading to a more pronounced spatial separation between the star and warm gas which it ionizes. In these regions, local ($d \lesssim 10$ pc for a single O3 star) sources supply ionizing photons. Examples of this include AFGL 2636, BD+43° 3654 and DR 16, DR 20, DR 22, and the complex environments of and between DR 17 and DR 23, with the notable distinction that all of these regions have not just one but a small cluster of massive OB stars within them. These regions are generally found at larger distances ($d \gtrsim 30$ pc) from Cyg OB2, to the east in the image. Likewise (single) massive field stars, for example to the northeast and southeast regions of the image, shape local filamentary structure.

Cyg OB2

To explore the role of Cyg OB2 in ionizing filamentary structure, we construct a map of the EUV (> 13.6 eV) ionizing photon rate per unit area from Cyg OB2, as shown in Figure 2.13, from catalogs of OB stars (Berlanas et al. 2018, and references therein). We describe how the map is created in detail in Appendix 2.B, following the procedure of Tiwari et al., in prep. Two important features of the map: (i) it is a simple 2D projection, and (ii) we do not attempt to account for any absorption or attenuation of ionizing photons. The total ionizing photon rate of the association from our model is 6×10^{50} EUV-photons s^{-1}, which we note agrees with the expectation of a zero age main sequence association with stellar mass $M_\star \approx 1.6 \times 10^4$ M$_\odot$ (Starburst99; Leitherer et al. 1999).

In Figure 2.13 we compare the ionizing photon flux from Cyg OB2 with the ionizing photon flux estimated directly from the optically thin thermal radio continuum at 1.4

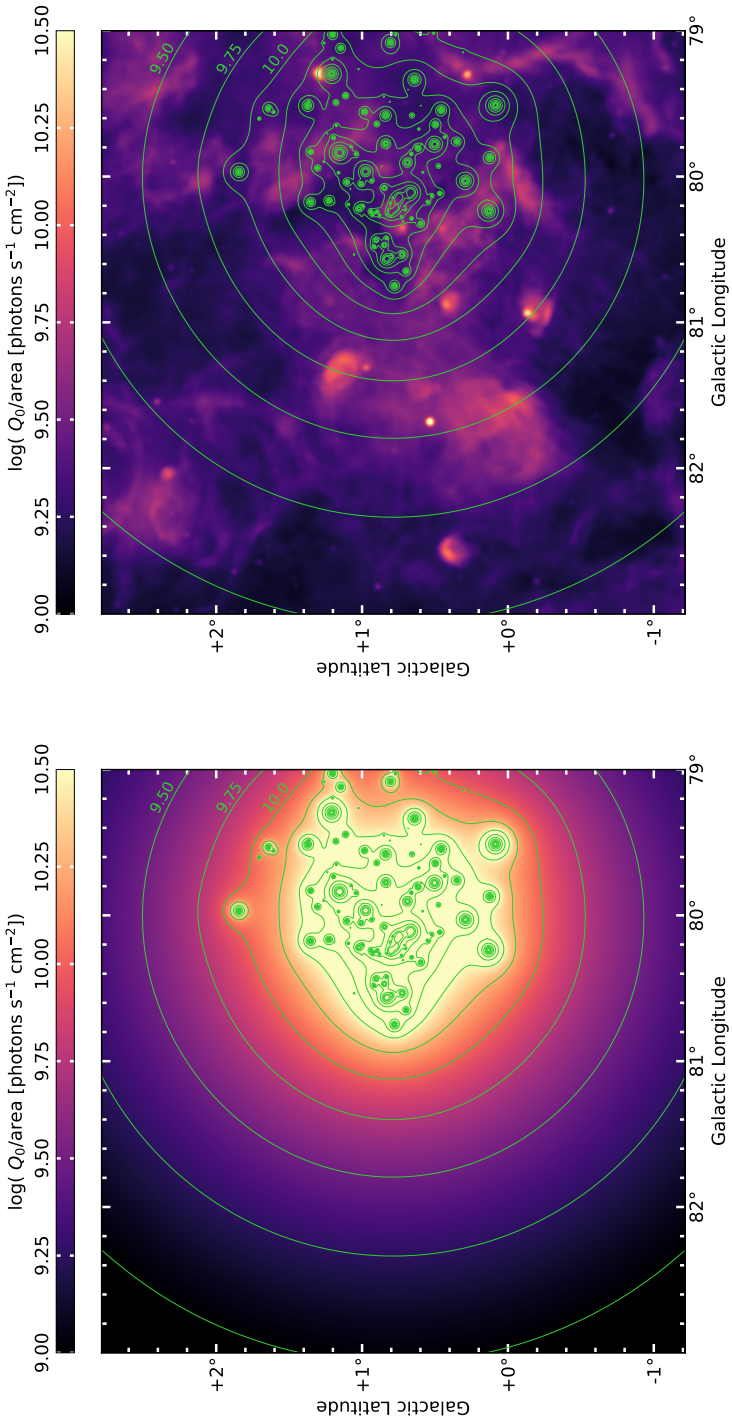

Figure 2.13: *Left:* A map of the ionizing photon (> 13.6 eV) rate per unit area constructed from the observed OB stars of the Cyg OB2 association (for details see Appendix 2.B). Green contours are shown at $\log(Q_0/\text{area [photons s}^{-1}\text{ cm}^{-2}]) = (9, 9.25, 9.5, \ldots 12.25)$. *Right:* The ionizing photon rate per unit area as traced by thermal free-free emission. The green contours of the Cyg OB2 ionizing field are overlaid.

GHz (e.g., Emig et al. 2020b),

$$Q_0/\text{area} = \left(1.998 \times 10^8 \text{ photons s}^{-1} \text{ cm}^{-2}\right) \left(\frac{EM}{10^3 \text{ pc cm}^{-6}}\right) \times \left(\frac{T_e}{10^4 \text{ K}}\right)^{-0.833-0.034 \ln(T_e/10^4 \text{ K})} . \tag{2.7}$$

The Cyg OB2 ionizing photon flux outshines a large portion of the inferred flux from the radio emission. We quantify how much of the low-density ionized gas can be maintained by the ionizing photons from Cyg OB2. We take the ratio of the two images shown in Figure 2.13, which equates to the observed ionizing photon flux divided by Cyg OB2's output ionizing photon flux. We compute that at 67% of the pixels in this region the ionizing photon flux from Cyg OB 2 is sufficient to maintain the ionization.

We make a rough comparison of the influence of Cyg OB2's ionizing radiation on filaments. Starting from the mask of the filament spines, we extend the mask at each filament segment to a square region of 29 pixel sides centered on the segment. This results in about a third of the pixels in the image being attributed to a filament. Taking the ratio of the images and considering only the masked pixels, we again find that for 67% of the pixels the ionizing photon flux from Cyg OB 2 is sufficient to provide the ionization.

We focus on some of the features and regions which appear to be influenced by Cyg OB2 in Figure 2.14. These radio continuum features correlate extremely well with 24 μm emission (see Figure 2.5) and do not appear to be directly related to individual H II regions. In Table 2.1 we include estimated properties of identified filaments. The widths, emission measures, and densities have been computed with the filament analysis described in Section 2.5. The length has been estimated by eye using the furthest extent of a straight line along a filament, starting and ending where the emission reaches a local intensity of half maximum. In this manner, the length of the curved features such as CXR 9a,b are slightly underestimated. We also compute the ionizing photon flux and the ionizing photon rate. In these filaments, the ionizing photon flux from Cyg OB2 at their projected distances is a factor of 10 or more than required.

Internal B stars?

The ionizing photon rates of the filaments exemplified in Table 2.1 are $\sim 2\times10^{48}$ EUV-photons s^{-1}, a rate which could be supplied by early type B stars local to the filaments. Wendker et al. (1991) argued for the filaments being internally ionized by about 3 to 10 stars of type B2 to B3. They give additional reasoning that filaments ionized externally are typically smaller, strongly curved, and with shallower intensity gradients at the edges. However, searches for B stars in these (low extinction) regions have subsequently been made and can now rule out the presence of (B) stars with confidence (Comerón & Pasquali 2012; Comerón et al. 2020). Furthermore, in Section 2.5 we mention examples of externally illuminated ionized filaments of similar length, width and curvature as the filaments observed in the Cygnus X region, and

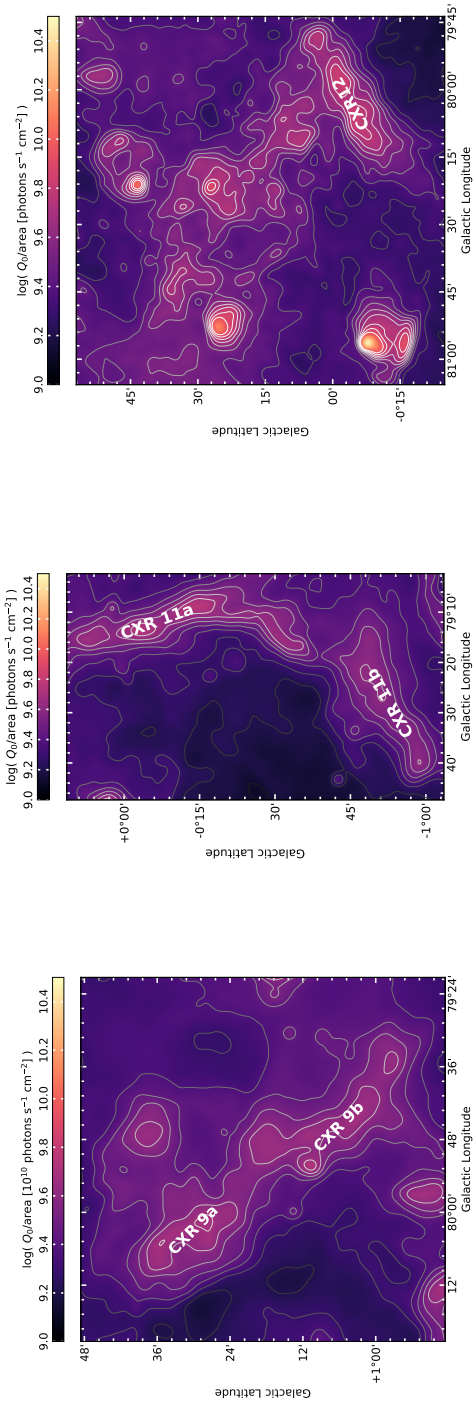

Figure 2.14: Here we show a zoom-in on filaments whose properties we discuss in more detail (see Table 2.1 and Sections 2.6.1 & 2.6.2).

Table 2.1: Properties of select filaments which are likely influenced by Cyg OB2.

Filament	Width (pc)	Length (pc)	EM (pc cm^{-6})	n_e (cm^{-3})	Q_0/area (10^9 photons s^{-1} cm^{-2})	Q_0 (10^{48} photons s^{-1})	M_+ ($M_\odot$)	D_{CygOB2} (pc)
CXR 9a	5.3	8.0	5600	33	1.4	2.8	740	19
CXR 9b	4.6	14.9	5600	35	1.4	2.1	1100	15
CXR 11a	3.6	14.7	7500	46	1.9	1.7	880	34
CXR 11b	4.6	13.8	4200	30	1.1	1.5	880	47
CXR 12	4.2	15.0	7800	43	2.0	2.4	1100	22

Width is the median FWHM width of all profiles of the filament.
Length is the by-eye estimate of the longest extent of the filament.
EM is the median peak emission measure over all profiles of the filament.
n_e is the median electron density estimated from all profiles of the filament.
Q_0/area is the median of the EUV ionizing photon flux estimated from all profiles of the filament.
Q_0 is the median of the EUV ionizing photon rate estimated from all profiles of the filament.
D_{CygOB2} is the approximate projected distance from Cyg OB2.

in the next section (Section 2.6.2), we extensively discuss evidence for the (external) mechanisms responsible for the forming of filaments.

2.6.2 Origin of the filaments

Photoevaporation

When an ionized volume of gas is not in (pressure) equilibrium with neutral gas, an ionization front propagates into the neutral medium. With increasing distance from the ionizing source, an ionization front is preceded by a layer of swept up neutral gas and somewhat further away an H_2 dissociation front (Elmegreen & Lada 1977). Since gas at the ionization front is over-pressured compared with the inner, low-density ionized gas, a flow occurs towards the ionizing source. The back-reaction created when the ionized gas pushes off the neutral material (the rocket effect) may eject even more mass and exert significant forces. Ionized gas with enhanced density (and intensity) is observed at this photoevaporating boundary. Photoevaporating surfaces are also referred to as ionized boundary layers and occur in champagne flows (Tenorio-Tagle 1979) and blister-like H II regions.

We sketch a rough portrait of the PDR like transition from ionized, atomic, to molecular gas at a photoevaporating surface (see (Hollenbach & Tielens 1999) and references therein). First we derive the width of the neutral region of the interface in order to compare the distribution and morphology of the ionized gas (3.6 pc width) and the PAH emission. Assuming the gas in the filaments is fully ionized up to the ionization front, the median thermal pressure is $P/k_{\rm B} = 2n_eT_e \approx 5.6 \times 10^5$ K cm^{-3}. The temperature of neutral material is $T \sim 100$ K at an extinction of $A_{\rm V} \sim 2$ mag. Assuming the ionized gas at this ionization front is in pressure equilibrium with neutral material, the gas would have a density $n_{\rm PDR} \sim 5600$ cm^{-3}. Adopting $\rm N_{PDR}/A_V = 2.1 \times 10^{21}$ cm^{-2} mag^{-1} (Zhu et al. 2017), then $N_{\rm PDR}/n_{\rm PDR} \approx 0.2$ pc. Thus, for these high pressures, we expect a relatively narrow region of approximately 0.2 pc (or 30″ for Cygnus X) of neutral gas bright in PAH emission between the ionized gas filament and the dissociation front. For less intense radiation or a less dense medium, the width of the neutral region extends further.

Photoevaporating boundaries are seen at the PDR interfaces traced by 8 μm emission in Figure 2.5 in more compact regions of star-formation that have local sources of intense radiation – e.g., filaments associated with sources AFGL 2636, DR 7, DR 17, DR 22 and DR 23. Other possible examples are the filaments which fall in the regions between DR 16 and DR 17 – where in Figure 2.5, emission is found surrounding massive stars but not overlapping with them.

For gas flowing away from the ionization front approximately at the sound speed, $C_{\rm H\ ii} \sim 10$ km s^{-1},[9] a filament of 3.6 pc would be visible for 0.4 Myr, but would continue eating away at the neutral clouds. An ionized mass of 940 $\rm M_\odot$, which is the mean value of the Table 2.1 entries, implies a mass loss rate of the neutral cloud of 2400 $\rm M_\odot$ Myr^{-1}. Each photoevaporating surface with these approximate characteristics would evaporate 1.2×10^4 $\rm M_\odot$ of ionized gas over the lifetime, ∼5 Myr,

[9] $c_{\rm s} = \sqrt{k_{\rm B}T/\mu m_{\rm H}}$, with μ the mean weight of the particles and $m_{\rm H}$ the mass of a hydrogen atom

of Cyg OB2. This mass is comparable to the stellar mass of Cyg OB2 and about 10% of the mass of a typical molecular cloud of 10^5 $M_\odot$ (Tielens 2005).

The properties of the filaments identified in Cygnus X are comparable with those of the California Nebula and the ionization front IC 434. The ionized filaments of the California Nebula have $EM = 2200$ pc cm^{-6} and FWHM size of 1.1 pc, and they arise from a single, high-velocity O star passing by and illuminating a molecular cloud some 50 pc away (e.g., Bohnenstengel & Wendker 1976). The ionization front IC 434 arises from a photoevaporating flow ionized by σ Ori with an emission measure of $EM = 2 \times 10^4$ pc cm^{-6} measured in Hα and also is about 1 pc wide (e.g., Ochsendorf et al. 2014). The densities computed for the California Nebula and IC 434 assuming $n_e = \sqrt{EM/\ell}$ are ∼44 and 47 cm^{-3}, respectively.

To determine if the filaments show a relationship to ionizing radiation, we estimate the dimensionless ionization parameter, U, and plot it as a function of density in Figure 2.15. Following Pellegrini et al. (2011), we define the ionization parameter from the ionizing photon flux and density as

$$U = \frac{Q_0}{\pi(\mathrm{width})^2 c n_e}. \tag{2.8}$$

The ionization parameter is indicative of the ratio between radiation and gas pressures. The electron density is expected to depend on U when its properties depend on the incident radiation field – also including when radiation pressure has influence. The ionization parameter has typical values of $U \gtrsim (10^{-2} - 10^{-3})$ in H II regions while the WIM has $U \sim 10^{-4}$ (e.g., Tielens 2005; Kewley et al. 2019). Because there is a general trend of increasing U as the density increases in our data, this indicates that ionizing radiation influences the filaments' properties. This would argue against stellar winds shock-heating the ionized gas and regulating the ionized gas pressure and density (see Section 2.6.2).

We mention a caveat in these calculations. If the "filaments" are truly photoevaporating surfaces, then their emission is more likely to be distributed in sheets rather than filaments, and thus traversing a pathlength along the line of sight. The electron densities of the ionized gas measured in this way would be about two times smaller, if we assume that the pathlength along the line of sight is equal to the longest dimension of the filament (which seems to be at most a factor of four longer than the width).

Looking at this scenario from a different perspective, we also discuss whether filaments that do not have or are significantly displaced from PAH or CO emission can plausibly be photoevaporating flows. The largest filaments, which are far from individual star-forming regions and may be influenced by Cyg OB2, have significant offsets between the ionized filament and neutral material (as traced by CO or 3.6,8 μm emission). Examples of this include CXR 12, CXR 11a,b, and the region just southeast of the Cyg OB2 core — all of which are shown in Figure 2.14. Using CXR 11b as an example, the projected distance between the ionized ridge and the PAH emitting ridge is $d \approx 7' \sim 3$ pc. The large separation would imply that the neutral gas is rather diffuse; the estimated density is $n_{\mathrm{PDR}} = \mathrm{N}_{\mathrm{PDR}}/d \sim 450$ cm^{-3}, since $\mathrm{N}_{\mathrm{PDR}} \approx 4.2 \times 10^{21}$ cm^{-2}. Pressure equilibrium, at $T \approx 100$ K would thus be $P/k_{\mathrm{B}} \sim 4.5 \times 10^4$ K cm^{-3}. For a temperature of 7400 K, the filament's ionized density is expected to be 6 cm^{-3}. Even if we assume CXR 11b is a sheet rather than a filament and we

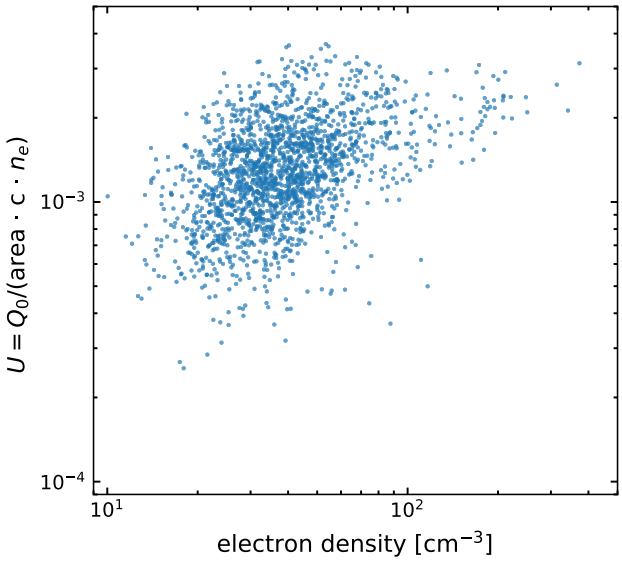

Figure 2.15: The dimensionless ionization parameter, U, estimated for each radial profile plotted against its electron density. The correlation between density and U indicates that the filament properties depend on the incident radiation field. No correlation as a function of density would indicate other (feedback) processes influence the physical properties (density) of the filaments.

let the pathlength along the line of sight equal the length along the plane of the sky, $\ell = 13.8$ pc, the electron density is still a factor of three too large, $n_e = \sqrt{EM/\ell} = 17$ cm^{-3}. In conclusion, ionized filaments that do not have neutral gas abutting the filament edge are likely not photoevaporating surfaces.

Stellar Winds

Next, we turn our attention to the strong stellar winds of Cyg OB2. Multiple interactions of the winds from massive stars produce diffuse shock-heated X-ray gas.[10] A region of hot ($T \gtrsim 10^6$ K) plasma fills the volume surrounding the star(s) at small radii. Swept-up interstellar gas is compressed at larger radii (e.g., Weaver et al. 1977; Harper-Clark & Murray 2009), forming a relatively dense shell of ionized gas and warm dust that is in pressure equilibrium with the hot gas.

A *Chandra* X-ray survey centered on Cyg OB2 has revealed a $R \approx 4.1$ pc cavity of hot ($T_X \approx 5 \times 10^6$ K) and diffuse ($n_X \approx 0.06$ cm^{-3}) gas (Albacete Colombo et al. 2018). In comparison, the core of Cyg OB2 marked with a gray circle in Figure 2.5, has a radius of $r = 34'$ ~15 pc. X-ray observations in the Cygnus X region are complicated by high levels of absorption (especially soft X-rays, which are dominated by wind-ISM interactions) in the Galactic plane; the total extent and intensity of the X-ray emission could reasonably be underestimated. Estimating the volume averaged pressure from hot gas, we find $P_X/k_B \approx 2n_X T_X \sim 6 \times 10^5$ K cm^{-3}, where n_X and T_X

[10] Any previous (generations of) supernovae would also contribute to shock-heated X-ray gas.

are the electron number density and temperature. This matches the median thermal pressure of the ionized filaments, which is what would be expected for ionized gas in pressure equilibrium with hot shocked gas.

There are several radio filaments abutting a cavity around the Cyg OB2 stars and where dense gas counterparts as traced through PAH or CO emission are not immediately obvious. The main region under consideration is shown in Figure 2.14,*left*; it stretches ∼32 pc in projection, ending in the southwest with CXR 12. As seen most clearly in Figure 2.5, the 24 μm emission (coincident with thermal radio emission) does not appear to be bordered by PAH emission at 8 μm. CO avoids the regions of ionized gas (warm dust), however CO is present in projection in some regions at larger radii. Another region to consider is CXR 9. While faint PAH emission and traces of CO emission are seen towards the south, in CXR 9b, dense gas does not seem the be related to CXR 9a. The regions in consideration are close to Cyg OB2 in projection, falling within about a 20 pc radius.

If the filaments (which are not associated with neutral gas) are influenced by stellar winds, they may be short-lived turbulent features. A correlation between the luminosity of giant ($r > 10$ pc) H II regions (and their size) and the line-width has been established (e.g., Terlevich & Melnick 1981), though the origin of the supersonic turbulence may be gravity-driven or (wind)feedback-driven. We note the ionized gas line-widths in the (resolved) filaments of Cygnus X are broader than the purely thermally broadened expectation. For example, the median ionized gas full width half maximum (FWHM) of the zoom-in regions of Figure 2.14, determined from H110α (4.8 GHz) observations, is $\Delta\mathrm{v} = 27$ km s^{-1} (Piepenbrink & Wendker 1988), whereas the Doppler-broadened thermal line-width[11] is $\Delta\mathrm{v}_{\mathrm{th}} = 16$ km s^{-1} (Brocklehurst & Seaton 1972). The rms turbulent velocity width is calculated as $\Delta\mathrm{v}_{\mathrm{rms}} = \sqrt{\Delta\mathrm{v}^2 - \Delta\mathrm{v}_{\mathrm{th}}{}^2} \sim 22$ km s^{-1} (Salgado et al. 2017b).

We determine the thermal energy in the hot gas as $E_{\mathrm{X}} = P_{\mathrm{X}}(\frac{4}{3}\pi R^3) \sim 7\times10^{47}$ erg. Using Starburst99 (Leitherer et al. 1999), the energy output from stellar winds of an $M_\star = 2\times10^4$ M$_\odot$ population of age 4 Myr is estimated at $E_{\mathrm{w}} \sim 3\times10^{52}$ erg. Since the mechanical energy of the wind is more than four orders of magnitude larger than the hot gas energy and theory predicts it should be roughly half (Weaver et al. 1977), the hot gas is likely venting into the medium. Judging also by the morphology of the gas, the hot gas does not appear to be entirely well contained. A possible vent may be the region to the North which seems to be devoid of gas and dust tracers – H II, CO, MIR, FIR.

Averaging the mechanical energy of the wind over the 4 Myr lifetime of the association, the rate of energy injection by the winds is estimated at $\dot{E}_{\mathrm{w}} \sim 2\times10^{38}$ erg s^{-1}. Let's compare that with the calculated energy dissipation rate in the potentially turbulent-induced filament. The (kinetic) energy in the observed filaments is $E_{\mathrm{fil}} = \frac{1}{2}M_+(\Delta\mathrm{v}_{\mathrm{rms}})^2 \sim \frac{1}{2}(940\ \mathrm{M}_\odot)(22\ \mathrm{km\ s}^{-1})^2 \sim 5\times10^{48}$ erg. Turbulent energy will be dissipated on a timescale comparable to the sound crossing timescale, $t = \mathrm{width}/\Delta\mathrm{v}_{\mathrm{rms}} \sim (3.6\ \mathrm{pc}\ /\ 22\ \mathrm{km\ s}^{-1}) \sim 0.2$ Myr. We calculate the energy dissipation rate (potentially) provided by filaments by bringing the energy and timescales

[11] $\Delta\mathrm{v} = (30.25\ \mathrm{km\ s}^{-1})\left(\frac{m_p}{m}\frac{T_e}{2\times10^4\ \mathrm{K}}\right)^{1/2}$ where $\Delta\mathrm{v}$ is the line FWHM, m_p is the proton mass and m is the nuclear mass (Brocklehurst & Seaton 1972).

together, $\dot{E}_{\rm fil} \sim 8 \times 10^{35}$ erg s^{-1}. Hence, we conclude that only $\sim 0.4\%$ of the mechanical energy in the stellar winds of the Cyg OB2 association is coupled to turbulent energy in the ionized gas.

2.6.3 Comparing filament properties with [N II] findings

In Section 2.6.2, we noted that the filament properties (EM, width, density) are consistent with filaments observed at photoevaporating surfaces of ionized boundary layers and stellar wind compressed ionized gas. Here we focus on a comparison of filament properties with ionized gas surveyed through [N II].

Ionized gas with electron densities distributed around 38 cm^{-3} appears to be consistent with ionized gas traced through the fine structure lines of [N II] at 122 and 205 μm with *Herschel* PACS (Goldsmith et al. 2015). Goldsmith et al. (2015) find a mean electron density of $n_e = 29$ cm^{-3} over 96 lines-of-sight of 16$''$ each in the Galactic midplane. While [N II] fine structure lines provide a reliable probe of the density of gas in the range $10 < n_e$ [cm^{-3}] $< 10^3$, only densities as large as 100 cm^{-3} were detected in their lines-of-sight. Detections of [N II] which fall just outside, $(\ell, b) = (78.1132°, 0.0°)$, of the region we analyze resulted in an electron density of $n_e = (13.0 \pm 1.7)$ cm^{-3}. Furthermore, a lower limit of $n_e \gtrsim 30$ cm^{-3} was derived from [N II] in the DR 21 region (White et al. 2010). Additionally, Pineda et al. (2019) derive the electron densities of 21 discrete spectral components using [N II] 205 μm and radio recombination lines. They find an average electron density of 41 cm^{-3} with values ranging from 8 to 170 cm^{-3}. The electron densities we find are in remarkable agreement and indicate that what we observe in the Cygnus X region with low-frequency radio emission may point to the types of environments which are traced by these [N II] surveys.

This conclusion is also supported by the H II column densities that Goldsmith et al. (2015) derives. They find [N II] column densities of $N(\mathrm{N}^+) = (1 - 20) \times 10^{16}$ cm^{-3}. Using their estimated nitrogen fractional abundance $X(\mathrm{N}+) = 2.9 \times 10^{-4}$, their column densities would translate into ionized hydrogen column densities of $N(\mathrm{H}^+) = (3 - 70) \times 10^{19}$ cm^{-3}. As shown in Figure 2.10, the column densities of ionized gas found in the [N II] survey are consistent with the column densities of filaments of ionized gas in the Cygnus X region.

2.6.4 Connection to ELD ionized gas

Extended low-density (ELD) ionized gas (Mezger 1978) has characteristic densities of $n_e = (5 - 10)$ cm^{-3} and pathlengths of (50–200) pc. In the region we investigate, diffuse thermal emission of $EM = 5300$ pc cm^{-6} is seen across the $\mathcal{O}$(100 pc) region. In addition to filling the Cygnus X region, emission may also arise along the line of sight, as we are looking down a spiral arm. Thus considering path-lengths of 0.1 – 1 kpc, the volume filling electron density is estimated at $n_e \approx (2 - 7)$ cm^{-3}. We take $n_e \approx 5$ cm^{-3} as a representative value, and note this is accurate to within a factor of two. The mass of ionized gas in the $R = 50$ pc volume we analyze is then 6×10^4 M$_\odot$ (or 2×10^5 M$_\odot$ in a Strömgren volume). Ionized gas of density $n_e \sim 5$ cm^{-3} and cloud size 100 pc are consistent with the properties of ELD ionized gas. Tying the volume-

filling ionized gas in Cygnus X with ELD ionized gas is consistent with previous results which connect ELD ionized gas to envelopes of H II regions (Shaver 1976; Anantharamaiah 1986; McKee & Williams 1997) and those which suggest ELD gas predominantly arises from the most massive regions of star formation in our Galaxy (Murray & Rahman 2010).

The thermal pressure felt by the volume filling warm ionized gas, for an electron temperature of $T_e \approx 7400$ K and a fully ionized medium, is $P/k_{\rm B} = 2n_eT_e \sim 7.4 \times 10^4$ K cm^{-3}. While this pressure is a factor of 10 lower than in the ionized filaments ($P/k_{\rm B} \sim 6 \times 10^5$ K cm^{-3}) and the X-ray emitting plasma, it is still elevated compared with the diffuse ISM ($P/k_{\rm B} \sim 4 \times 10^3$ K cm^{-3}) (Jenkins et al. 2011). Overpressurization is consistent even for the globally elevated ISM pressure expected in spiral arms and at small galactic radii (Wolfire et al. 2003).

In the Cygnus X region, ELD ionized gas is filled and replenished by photoevaporating filaments (similar in properties to [N II] gas of (Goldsmith et al. 2015; Pineda et al. 2019)) eroding neutral clouds over the lifetime of the massive stars. As we calculated in Section 2.6.2, a characteristic filament in the region photoevaporates 1.2×10^4 M$_\odot$ of cloud mass over the lifetime of the massive stars. Five of the characteristic filaments supply an equal mass of ionized gas in the region analyzed, and ten filaments would replenish the full Strömgren volume.

2.6.5 Future LOFAR observations

Our results have demonstrated new capabilities provided by LOFAR to characterize low-density ionized gas at low radio frequencies and high spatial resolution. Our analysis indicates that observations making use of the full bandwidth of data for a typical LOFAR HBA observation would reach noise levels of (25 mJy beam^{-1})/$\sqrt{20}$ = 5 mJy beam^{-1} or free-free emission measures of 160 pc cm^{-6} at a resolution of 2′, reaching similar EM depths as the CGPS 1.4 GHz observations. Future investigations in conjunction with LOFAR's LBA at 30–80 MHz will enable ionized gas (with typical ionized gas temperatures of 7000 K) to be characterized with free-free optical depths down to ∼400 pc cm^{-6}. With the LOFAR Survey (Shimwell et al. 2019), the Galactic Plane in the Northern hemisphere will be covered to a spatial resolution of up to 6″. Our analysis, builds on previous LOFAR analyses (e.g., Arias et al. 2019), which show the power of LOFAR to characterize the continuum emission at low radio frequencies in the Galaxy.

2.7 Conclusions

Photoionized gas probes the influence of massive stars on their environment. The Cygnus X region ($d \sim 1.5$ kpc) is one of the most massive star forming complexes in our Galaxy, in which the Cyg OB2 association (age of 3–5 Myr and stellar mass of $M_\star \approx 2 \times 10^4$ M$_\odot$) has a dominant influence. We observed the Cygnus X region at 142 MHz using LOFAR and corrected for missing short-spacing information during image deconvolution. Together with archival data from the Canadian Galactic Plane Survey, we investigate the morphology, distribution, and physical conditions of low-

density ionized gas in a $4^\circ \times 4^\circ$ ($\sim$100 pc $\times$ 100 pc) region at a resolution of $2'$ (0.9 pc). As first discussed at radio frequencies by Wendker et al. (1991), the ionized gas in this region is characterized by filamentary structure. We use the `DisPerSE` and `FilChaP` packages to characterize the radial profiles of low-density ionized filaments. Our results are as follows:

- We have demonstrated a procedure for correcting for a lack of short-spacing information in LOFAR observations. We compare our results with feathering and find them to be consistent within 6% (on average) across the region analyzed, thanks to LOFAR's excellent sensitivity to large scale emission. Future LOFAR HBA observations, especially together with the LOFAR LBA at 30–70 MHz, will characterize the low-density ISM to deep emission measures and high spatial resolution.

- Radio continuum emission in the region is largely consistent with free-free thermal emission down to our LOFAR observing frequency of 142 MHz. This agrees well with previously analyses down to 408 MHz (Wendker et al. 1991; Xu et al. 2013).

- The low density ionized gas traced by the radio continuum shows a strong correspondence with warm dust traced by 24 μm emission.

- We fit free-free optical depths at 142 MHz in diffuse, extended (2° scale) emission with values of $\tau_{\rm ff} = (0.1 - 1.5)$, corresponding to emission measures of $EM = (2 - 40) \times 10^3$ pc cm^{-6}. While in four compact, unresolved regions of active star formation (DR 7, 15, 21, 22), we measure $\tau_{\rm ff} > 4$.

- We characterize 1934 EM radial profiles from 906 filaments. We find a power-law distribution in peak EM down to our completeness limit of 4200 pc cm^{-6}. A characteristic width of 3.6 pc arises in the distribution, well separated from our spatial resolution of 0.9 pc. The median electron density within the filaments is 38 cm^{-3} — quite similar to the ionized gas probed along the Galactic plane through [N II] (e.g., Goldsmith et al. 2015; Pineda et al. 2019). We derive thermal pressures within a median value of 6×10^5 K cm^{-3}, indicating the filaments are over-pressured compared with the neutral ISM.

- We construct an ionizing photon map of the Cyg OB2 association and compare it with the ionizing photon flux measured from the thermal radio continuum. We find that the ionizing photon flux from Cyg OB2 is sufficient to maintain ionization in 67% of the region and the filaments.

- We estimate that the (high-pressure) filaments are likely photoevaporating surfaces flowing into volume-filling warm ionized gas that is relatively low in pressure (with density $n_e \sim 5$ cm^{-3}). We notice a correlation between the ionization parameter, U, and electron density, indicating filaments are primarily influenced by stellar radiation. We estimate that typical photoevaporating surfaces influenced by Cyg OB2 each convert $\sim 2 \times 10^4$ M$_\odot$ of neutral material (or 10% of a typical $\sim 10^5$ M$_\odot$ molecular cloud) into ionized gas over the lifetime of the association.

- A minority of filaments do not have or are significantly displaced from neutral gas (as traced by PAH and CO emission). We estimate the influence of stellar winds from Cyg OB2 and find that ∼0.4% of the mechanical energy in the winds may be coupled to turbulent energy in the ionized gas. In which case, some of the ionized filaments may be transitory features resulting from dissipated turbulence.

- The volume-filling ionized gas in the Cygnus X region — $M_+ \sim 2 \times 10^5$ $M_\odot$ with $n_e \sim 5$ cm^{-3} and ∼100 pc pathlength — is consistent with properties of extended low-density (ELD) ionized gas (Mezger 1978) and connects to previous findings which attribute ELD ionized gas to envelopes of H II regions and those which suggest the most massive star forming regions likely dominate ELD emission. ELD ionized gas which leaks from this largely inhomogeneous region can be replenished in mass by ∼10 (typical) photoevaporating surfaces over the ∼ 5 Myr lifetime of the OB stars.

Acknowledgements

We thank Nicola Schneider for sharing data products, and Frits Sweijen and Alex Mechev for maintaining software on the grid infrastructure and in Leiden. KLE thanks the Green Bank Observatory for the hospitality as hosting her as a (remote) guest during the completion of this work.

KLE, HJAR and AGGMT acknowledge financial support from the Dutch Science Organization (NWO) through TOP grant 614.001.351. GJW gratefully acknowledges the support of an Emeritus Fellowship from the Leverhulme Trust. AGGMT acknowledges support through the Spinoza premier of the NWO. Part of this work was carried out on the Dutch national e-infrastructure with the support of the SURF Cooperative through grant e-infra 160152.

This paper is based (in part) on results obtained with International LOFAR Telescope (ILT) equipment under project codes `LC0_032`. LOFAR (van Haarlem et al. 2013) is the Low Frequency Array designed and constructed by ASTRON. It has observing, data processing, and data storage facilities in several countries, that are owned by various parties (each with their own funding sources), and that are collectively operated by the ILT foundation under a joint scientific policy. The ILT resources have benefited from the following recent major funding sources: CNRS-INSU, Observatoire de Paris and Universite d'Orleans, France; BMBF, MIWF-NRW, MPG, Germany; Science Foundation Ireland (SFI), Department of Business, Enterprise and Innovation (DBEI), Ireland; NWO, The Netherlands; The Science and Technology Facilities Council, UK; Ministry of Science and Higher Education, Poland. The research presented in this paper has used data from the Canadian Galactic Plane Survey, a Canadian project with international partners, supported by the Natural Sciences and Engineering Research Council.

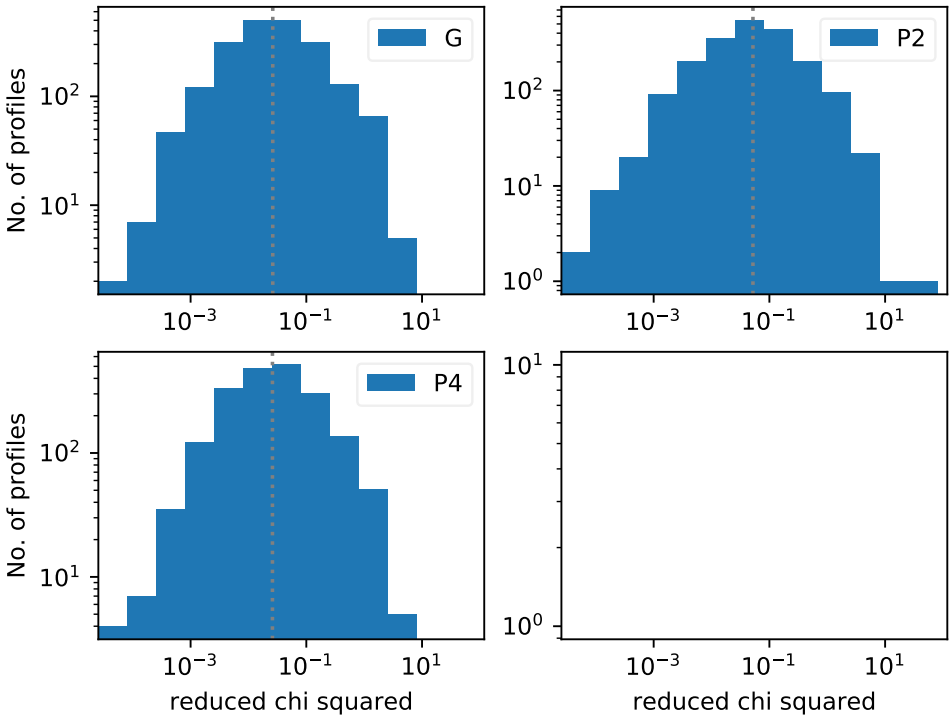

Figure 2.16: Reduced χ^2 distributions from mean radial profile fits. The four panels represent the distribution resulting from Gaussian fits (G; top left panel), Plummer $p = 2$ profile fits (P2; top right panel), and Plummer $p = 4$ profile fits (P4; bottom left panel). Broadly speaking the results between the fits are consistent, with Plummer $p = 4$ resulting in the lowest median value in the reduced χ^2 distribution.

2.A Additional fits to filament radial profile

We plot the histograms of the reduced χ^2 of fits to the filament radial profiles, for Gaussian and Plummer ($p = 2, 4$) profiles (Figure 2.16). We also show histograms with the results of those fits: the peak (Figure 2.17) and the FWHM width (Figure 2.18).

2.B Ionizing Photons from Cyg OB2

Using the procedure laid out in Tiwari et al., in preparation, we estimate the ionizing photon rate per unit area from early-type Cyg OB2 cluster members by synthesizing a list of stars from catalogs by Wright et al. (2015) and Berlanas et al. (2018, 2020), who in part used the catalog of Comerón & Pasquali (2012). All stars from these catalogs have effective temperatures and luminosities assigned from spectroscopic analyses. We take the assigned parameters from Berlanas et al. (2018, 2020) if possible, then from Wright et al. (2015), and finally Comerón & Pasquali (2012) via Berlanas et al.

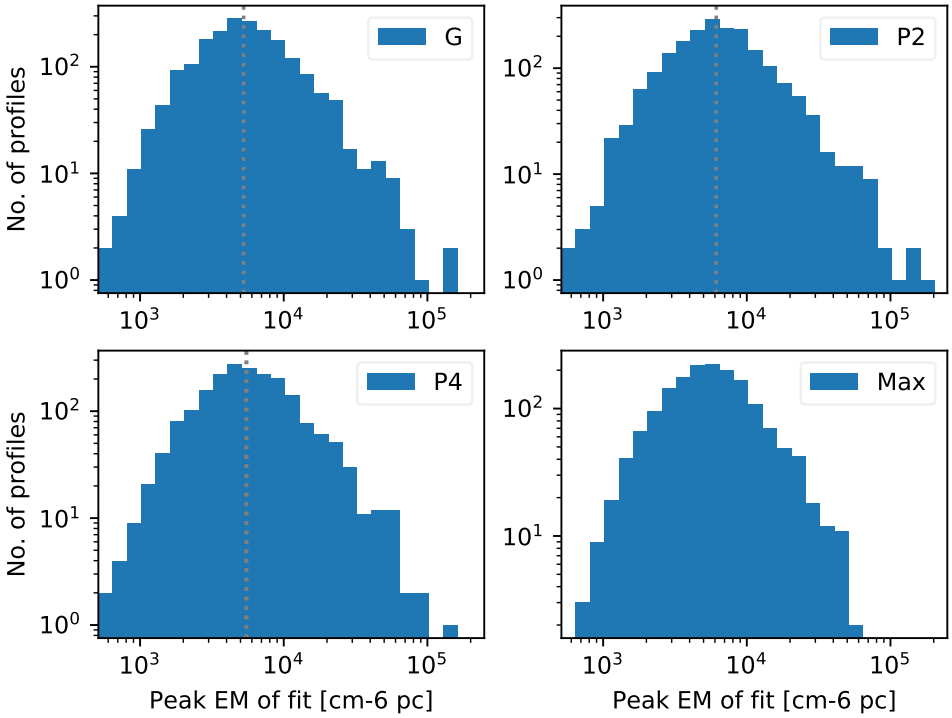

Figure 2.17: Peak EM distributions from mean radial profile fits. The four panels represent the distribution resulting from Gaussian fits (G; top left panel), Plummer $p = 2$ profile fits (P2; top right panel), Plummer $p = 4$ profile fits (P4; bottom left panel), and the maximum value of the profile (Max; bottom right panel). The median value of the EM distributions is robust to different determinations.

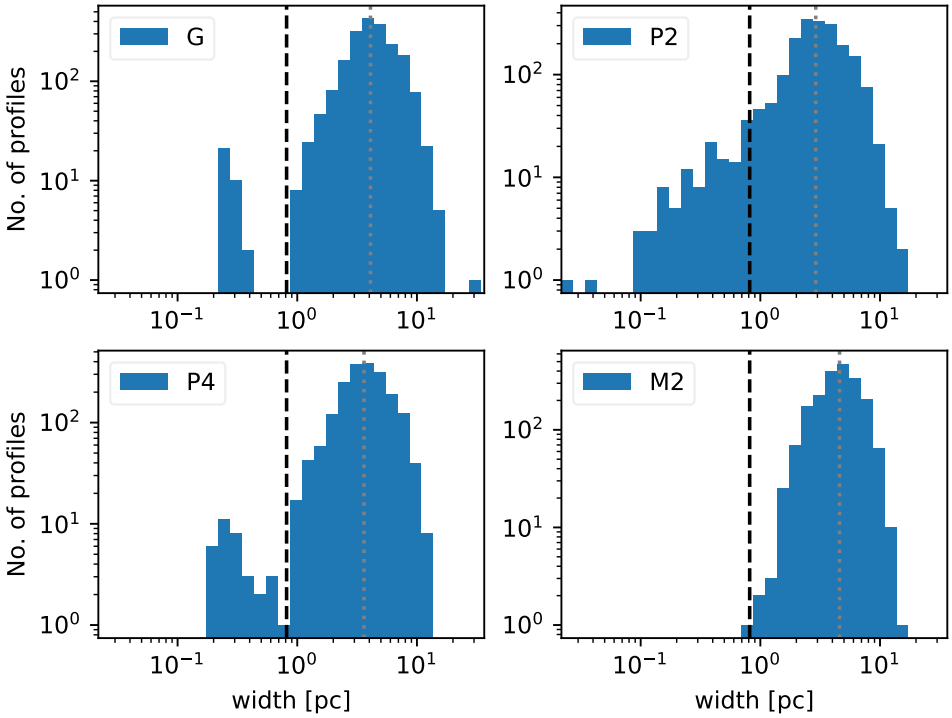

Figure 2.18: Width distributions from mean radial profile fits. The four panels represent the distribution resulting from Gaussian fits (G; top left panel), Plummer $p = 2$ profile fits (P2; top right panel), Plummer $p = 4$ profile fits (P4; bottom left panel), and the moment 2 computed width (M2; bottom right panel). A peak in the width distribution is seen across all four different width determinations.

(2018). With these effective temperatures and luminosities, we pick out models for each O or B star from the Potsdam Wolf-Rayet (PoWR) stellar atmosphere grids (Hamann & Gräfener 2004; Todt et al. 2015; Sander et al. 2015; Hainich et al. 2019). These models are gridded by effective temperature and gravity, so we first interpolate the gravity, $\log g$, from the grid's associated temperature and luminosity values. From the synthetic spectra provided by the PoWR models, we integrate the total ionizing flux above 13.6 eV. We then use the stellar coordinates and the ionizing photon flux to estimate the ionizing photon rate per unit area at any location around the H II region using projected distances at 1.5 kpc and summing over the flux from all stars.